Finite slip models of the 2019 Ridgecrest earthquake sequence constrained by space geodetic data and aftershock locations

Zeyu Jin and Yuri Fialko

Institute of Geophysics and Planetary Physics, Scripps Institution of Oceanography, University of California, San Diego, La Jolla, CA 92023, USA

Corresponding author:
Zeyu Jin
email: `zej011@ucsd.edu`

Abstract

The July 2019 Ridgecrest, California earthquake sequence involved two large events, the M6.4 foreshock and the M7.1 mainshock that ruptured a system of intersecting strike-slip faults. We present analysis of space geodetic observations including Synthetic Aperture Radar (SAR) and Global Navigation Satellite System (GNSS) data, geological field mapping, and seismicity to constrain the sub-surface rupture geometry and slip distribution. The data render a complex pattern of faulting with a number of sub-parallel as well as cross-cutting fault strands that exhibit variations in both strike and dip angles, including a "flower structure" formed by shallow splay faults. Slip inversions are performed using both homogeneous and layered elastic half space models informed by the local seismic tomography data. The inferred slip distribution suggests a moderate amount of the shallow coseismic slip deficit. The peak moment release occurred in the depth interval of 3-4 km, consistent with results from previous studies of major strike-slip earthquakes, and the depth distribution of seismicity in California. We use the derived slip models to investigate stress transfer and possible triggering relationships between the M7.1 mainshock and the M6.4 foreshock, as well as other moderate events that occurred in the vicinity of the M7.1 hypocenter. Triggering is discouraged for the average strike of the M7.1 rupture (320 deg), but encouraged for the initial orientation of the mainshock rupture suggested by the first motion data (340 deg.). This lends support to a scenario according to which the earthquake rupture nucleated on a small fault that was more optimally oriented with respect to the regional stress, and subsequently propagated along the less-favorably oriented pre-existing faults, possibly facilitated by dynamic weakening. The nucleation site of the mainshock experienced positive dynamic Coulomb stress changes that are much larger than the static stress changes, yet the former failed to initiate rupture.

Introduction

The 2019 Ridgecrest, California earthquake sequence initiated on July 4 with a strong $M_w6.4$ foreshock followed by a $M_w7.1$ mainshock on July 5. The $M_w7.1$ (hereafter, we drop the subscript w and refer to the earthquake magnitude as to the moment magnitude, unless otherwise noted) mainshock was the largest event that struck California

1

over the last 20 years, since the 1999 Hector Mine earthquake (Barnhart et al., 2019; Chen et al., 2020; Liu et al., 2019; Ross et al., 2019). The epicentral area of the 2019 earthquake sequence is located between the town of Ridgecrest to the south-west, the Searles Valley to the east, and the Garlock fault to the south (Figure 1). Faults that produced the foreshock and the mainshock, as well as their numerous aftershocks, were not previously recognized as continuous connected features capable of producing a major earthquake, but appear to be spatially associated with the Little Lake fault zone. The latter is in turn part of the Eastern California Shear Zone (ECSZ), a complex network of active Quaternary faults that accommodates between 10 and 20% of the relative motion between the Pacific and North American plates (Dokka and Travis, 1990; McClusky et al., 2001; Sauber et al., 1986; Tymofyeyeva and Fialko, 2015). It has been proposed that the ECSZ represents an incipient plate boundary forming in response to the development of a major restraining bend in the San Andreas fault system to the west (Nur et al., 1993). Indeed, all of the major ($M7+$) earthquakes that occurred in southern California over the last 50 years were located in the ECSZ (e.g., Fialko, 2004; Fialko et al., 2001; Hauksson et al., 2002; Sieh et al., 1993; Simons et al., 2002).

The M6.4 foreshock activated a left-lateral northeast (NE) trending fault, and possibly a 10-20 km long segment of a right-lateral NW trending fault that was subsequently ruptured by the M7.1 mainshock (e.g., Ross et al., 2019). The mainshock nucleated $\sim$ 15 km to the NW of the foreshock epicenter and bilaterally propagated along a system of previously mapped and unmapped right-lateral faults striking NW. Most of the M7.1 rupture occurred within the boundaries of the US Naval Air Weapons Station (NAWS) at China Lake. The most recent (prior to 2019) activity in the Ridgecrest area involved a series of moderate to strong earthquakes in 1995-1996 (Hauksson et al., 1995), some of which occurred within just a few kilometers from the epicenter of the mainshock of the 2019 sequence. This clustering of seismic activity, combined with large volumes of high-quality observations, makes the Ridgecrest sequence a good target for investigations aimed at improving our understanding of the mechanisms of spatio-temporal earthquake clustering, stress-mediated earthquake interaction, and triggering. In this paper we use a rich combination of space geodetic, geologic, and seismic observations to derive finite slip models of the 2019 foreshock-mainshock sequence. We then apply these models to investigate the role of static and dynamic stress changes and stress heterogeneity in the earthquake triggering.

Data and Methods

The 2019 Ridgecrest earthquakes occurred in the middle of dense instrumental networks, including the Plate Boundary Observatory (Herring et al., 2016), and the Southern California Seismic Network (Hauksson et al., 2001). They were also well imaged by a number of currently active satellite missions with Interferometric Synthetic Aperture Radar (InSAR) capabilities, including C-band Sentinel-1A/B, L-band ALOS-2, and X-band Cosmo-Skymed (see Figure 1 for data coverage). This, together with nearly-optimal surface conditions for InSAR (arid semi-desert with sparse vegetation) and a rapid field response including geologic, geodetic, and seismic components resulted in a comprehensive data set that makes the 2019 Ridgecrest earthquake sequence one of the best-documented seismic events to date. Large volumes of high-quality data

enable modeling of the earthquake sources with increasing accuracy and resolution. In this section we describe the data sets that were used to inform our models of the Ridgecrest earthquakes.

SAR data

High-quality SAR data from different look directions are in principle sufficient to completely describe surface displacements due to large shallow earthquakes (e.g., Fialko, 2004; Fialko et al., 2005b; 2001). Such data were acquired over the Ridgecrest area shortly before and after the foreshock/mainshock sequence by a number of satellite missions (Figure 1). Because the two largest events occurred within just one day of each other, the timing of SAR acquisitions allows measurements of combined displacements from the M6.4 and M7.1 events, and not from either event individually. In Section "Stress changes due to the M6.4 foreshock and possible triggering of the M7.1 mainshock" we show that it may be possible to separate contributions to surface deformation from the foreshock and the mainshock given a well-resolved slip model for the composite event.

SAR data that most tightly bracket the earthquake dates were acquired by the Sentinel-1A and 1B satellites of the European Space Agency (see Table 1 and red frames in Figure 1). Sentinel-1A/B satellites operate using C-band (radar wavelength of 56mm) in the Terrain Observation by Progressive Scan (TOPS) mode, which allows for wide ($\sim$ 250km) swaths and short (minimum of 6 day) repeat intervals. Image pairs that span the earthquake dates are available from both the ascending and descending satellite orbits, providing different look directions, and a complete coverage of an area around the earthquake ruptures and beyond (Figure 1). A comparable coverage is also provided by the ALOS-2 mission of the Japanese Space Agency (Figure 1, blue frames) that operates in the ScanSAR mode on the ascending tracks. ALOS-2 uses an L-band radar (wavelength of 0.24m) that can provide a better coherence compared to C-band in areas affected by decorrelation (e.g., due to vegetation or intense damage near the surface rupture). We did not find this to be the case for the Ridgecrest sequence, possibly because the effect of a larger wavelength was offset by longer revisit intervals (Table 1), resulting in larger temporal decorrelation (e.g., Ahmed et al., 2011).

Even though the ALOS-2 interferograms do not provide an increased diversity in look directions compared to the Sentinel-1 data, the former are useful in that they are affected by errors (mostly, the propagation delays) that are independent from those in the Sentinel-1 data. We complement the Sentinel-1 and ALOS-2 observations with SAR data from the Cosmo-Skymed satellites that operate in stripmap mode using X-band (wavelength of 31mm). Because of the limited swath width and relatively sparse acquisitions, the Cosmo-Skymed data provide only a partial coverage of the rupture area (Figure 1, green frames), and are highly affected by decorrelation of the radar phase. However, a smaller pixel size, especially in the azimuth direction (by almost an order of magnitude, compared to Sentinel-1 and ALOS-2 data), makes the Cosmo-Skymed data useful for constraining the north-south component of the coseismic displacement field that is not well resolved by the Sentinel-1 and ALOS-2 measurements.

To minimize possible contributions from postseismic deformation (Barbot et al., 2008b; Gonzalez-Ortega et al., 2014; Johnson et al., 2006; Wang and Fialko, 2014; 2018), we considered post-earthquake scenes that were acquired within 20 days after

the mainshock. Analysis of the near-field GNSS data indicated that post-seismic displacements did not exceed a few tens of millimeters in the months following the earthquakes (Floyd et al., 2020) and are therefore negligible compared to the coseismic displacements. The pre-seismic scenes were chosen to minimize the time span and perpendicular baselines of the coseismic pairs. The resulting data set is summarized in Table 1.

All interferometric pairs were processed using GMTSAR (Sandwell et al., 2011). The topography contribution to the radar phase was calculated and removed using digital elevation data from the Shuttle Radar Topography Mission (SRTM) with 30 m resolution (Farr and Kobrick, 2000). The images were co-registered using a geometric alignment. Even in case of a perfect alignment, meter-scale surface displacements near the earthquake rupture introduce phase discontinuities across the burst boundaries in Sentinel-1 interferograms. Because the observed phase discontinuities across the burst boundaries are small, here we simply neglect them. In general, such discontinuities can be removed using a coseismic model to compute a range- and azimuth-dependent alignment, similar to corrections for the ionospheric perturbations (e.g., Wang et al., 2017).

To avoid artifacts due to unwrapping errors in the near field of the earthquake ruptures (where the decorrelation noise can be large), we unwrapped the radar phase using a conservative branch-cut algorithm (Goldstein et al., 1988). The resulting line of sight (LOS) displacements are shown in Figures 2a-d. To quantify surface displacements in the near field of the earthquake ruptures where the radar phase cannot be confidently unwrapped due to decorrelation, we computed range offsets using Sentinel-1 data (Figure 2e-f), and azimuth offsets using Cosmo-Skymed data (Figure 2g-h). While the offsets are less accurate compared to the differential radar phase, they are useful for locating the rupture and constraining the distribution of slip in the shallow crust. Because the azimuth pixel size for Sentinel-1 TOPS mode is almost an order of magnitude larger than the range pixel size, the Sentinel-1 azimuth offsets have a low signal to noise ratio (SNR), and are not used for slip inversions. We performed a quality check on all of the scenes used in the inversions, and manually masked out a few areas that were strongly affected by local errors or noise.

GNSS data

The Ridgecrest earthquakes occurred in an area spanned by the Plate Boundary Observatory, a mature network of continuously recording GNSS sites. This gave rise to a large set of well-constrained vector coseismic displacements. However, because the average spacing between continuous GNSS (cGNSS) sites of PBO is on the order of 10-20 km, the cGNSS data primarily constrain integral characteristics of seismic sources such as the moment tensor and/or the scalar moment. In order to densify the GNSS coverage in the near field, teams from the University of California San Diego, University of California at Riverside, University of Nevada at Reno, and the US Geological Survey coordinated a post-event response to occupy existing geodetic benchmarks within ~ 50 km from the earthquake rupture. Most of the selected benchmarks have been surveyed multiple times over the last 30 years, and some were surveyed as recently as several months prior to the July 2019 earthquakes (Floyd et al., 2020). We have collected post-event data from 7 campaign sites: 0806, INYO, GS11, GS17, GS20, GS22, and GS48. Some of the surveyed sites had benchmarks consisting of metal rods

driven or cemented into the ground, with center markings, that required a tripod setup (Figure 3a). At other sites, benchmarks consisted of a threaded pin encastered in a concrete block. For such sites, a GNSS antenna can be attached directly to a pin, without the need for a tripod (Figure 3b).

The data were collected at 15 second sampling intervals, and RINEX files were archived at UNAVCO (Fialko et al., 2019b). Following the post-event deployment, we left the sites running to document the early post-seismic deformation transient (Fialko et al., 2019a). Solutions for coseismic displacements derived from the campaign GNSS measurements were presented in Floyd et al. (2020). We use the coseismic offsets derived from campaign as well as continuous GNSS data (Floyd et al., 2020) along with data described in sub-section "SAR data" in joint inversions for the static slip models, as described in the next section.

Joint inversions of surface displacement data

In order to prepare the InSAR data for inversions for the sub-surface slip distribution, we de-trended the interferograms using low-resolution inverse models. A wide-swath capability of Sentinel-1 and ALOS-2 ensures that coseismic interferograms extend into areas where coseismic displacements are negligible (Figure 1). The satellite orbits are known sufficiently well such that the orbital errors should not introduce significant long-wavelength trends in the data. However, we find that the long-wavelength trends are often present, possibly due to propagation effects (e.g., regional variations in the troposphere and/or ionosphere) and need to be accounted for. Even in the absence of the long-wavelength artifacts, one needs to estimate the phase ambiguity corresponding to the far-field ("zero") displacements. We do so by performing inversions for the slip distribution and the best-fitting linear (or, in case of ALOS-2, higher order) ramps in the radar phase using coarsely discretized fault models and coseismic interferograms (e.g., Fialko, 2004). In these preliminary inversions we limited the fault depth to 15 km, based on the depth distribution of seismicity (e.g., Ross et al., 2019) to avoid trade-offs between spurious deep slip and the ramp coefficients, and assigned relatively heavy weights to the cGNSS data. The best-fit ramps were subtracted from the radar interferograms. Because the range offsets represent the same projection of the surface displacement field as the radar interferograms, we de-trended the range offsets by fitting a linear ramp to the residual between the detrended radar interferograms and the offsets, for each of the satellite tracks. The estimated ramps were subtracted from the range offsets, so that the latter have the same asymptotic behavior in the far field as the detrended interferograms and the cGNSS data. The azimuth offsets from Cosmo-Skymed were not included in the initial inversions because of a narrow swath that may not extend into a region of vanishing coseismic displacements (Figure 1). De-trending of the azimuth offsets was performed at the next stage using a refined slip model. The azimuth offsets thus provide independent constraints only on the shallow (depth < 5 km) part of the slip model, as intended.

The de-trended interferograms and range and azimuth offset maps were sub-sampled using a quad-tree algorithm (Jonsson et al., 2002; Simons et al., 2002). To avoid oversampling in areas affected by high-frequency noise (atmospheric contributions, unwrapping errors, phase decorrelation, etc.), we down-sampled the data iteratively using model predictions (Wang and Fialko, 2015). Following an initial inversion in

which the best-fit slip model was obtained, the location of the data samples was determined by executing the gradient-based quad-tree algorithm on a model prediction. The obtained resolution cells were populated by the mean values of data from the original de-trended interferograms. Usually, two or three iterations are sufficient to achieve a convergent set of data points. In order to capture the details of slip distribution near the Earth's surface, we more densely sampled the offsets data around the fault traces. In particular, given the patch size of ~ 1 km at the shallowest part of the slip model, we sampled the near-field data starting with the minimum resolution cell of ~ 250 m. The (spatially variable) unit look vectors for all data samples were computed by averaging the original values in the same resolution cells as used for sub-sampling the displacement data.

The sub-surface fault geometry is typically not well known, and is usually either assumed or estimated as part of a non-linear inversion of surface displacement data (e.g., Fialko, 2004; Simons et al., 2002). However, in case of the Ridgecrest earthquakes, data from a dense seismic network and advanced processing algorithms provided a catalog of accurately located aftershocks (e.g., Ross et al., 2019) that can be used to infer the rupture geometry throughout the seismogenic zone, under the assumption that aftershocks are illuminating the ruptured faults and/or their immediate neighborhood. We approximate the ruptures that produced the M6.4 foreshock and the M7.1 mainshock by a set of rectangular fault segments that honor multiple available data sets, including the aftershock locations (Ross et al., 2019), geologically mapped fault traces (Ponti et al., 2020), and surface offsets from the space geodetic imaging (Figure 2). The inferred geometry is illustrated in Figure 4 (also, see Supplemental Figures S3-S4).

Notable features of the aftershock distribution are: (i) change in the dip angle around the epicenter of the M7.1 event, with a steep SW dip in the northern part of the rupture, and a NE dip in the southern part; (ii) two sub-parallel NW-trending strands of seismicity in the southern section; (iii) clear offsets between the surface rupture trace and the projection of the aftershock cloud toward the surface in the central part of the rupture (shown by the dotted and solid black lines, respectively, in Figure 4a). We interpret this offset as a shallow splay structure that connects the surface rupture to the main fault strand at depth that is expressed in the aftershock activity (Figure 4b). The shallow dipping splay fault is not expressed in microseismicity, as is the "main" rupture in the shallow crust, presumably because of the velocity-strengthening conditions at low temperature and normal stress (e.g., Barbot et al., 2009a; Marone and Scholz, 1988; Mitchell et al., 2016; Rice and Tse, 1986). As we show below, the shallow splay structure has nevertheless produced a large coseismic offset. The data shown in Figure 4 also suggest that except for numerous cross-faults, the NW-striking fault at depth is quite linear and exhibits less variability in strike compared to the surface expression of the earthquake rupture.

We extended the rectangular segments approximating the fault geometry to the depth of 25 km, and by several km beyond the mapped fault traces along-strike, and sub-divided each segment into slip patches which sizes gradually increase from about 1 km (along-strike and down-dip) at the top of the fault to about 5-10km at the bottom, following a geometric progression to ensure that the model resolution does not decrease with depth (Fialko, 2004). We computed Green's functions for the strike and dip components of slip on each patch for every observation point. As there are many more data points than the degrees of freedom, the system is over-determined

and is solved by minimizing the L_2 norm of the residual. We applied a positivity constraint on strike-slip components, such that no slip on the NE-trending segments was allowed to be right-lateral, and no slip on the NW-trending segments was allowed to be left-lateral. No positivity constraints were imposed on the dip-slip components, but the latter were more strongly smoothed compared to the strike-slip components to avoid spatially oscillating slip patterns. The first-order Tikhonov regularization (e.g., Golub et al., 1999) was applied to avoid extreme variations in slip between the adjacent fault patches. This also refers to complex intersections between different fault segments (e.g., between the shallow splay faults and the main fault), in which case the "neighboring" patches were identified based on a distance between the patch edges.

We further regularized the problem by imposing "soft" zero-slip boundary conditions ($wS{=}0$, where S is an unknown slip magnitude, and w is a prescribed weight) at the fault edges, except for most of the edges at the free surface that were left unconstrained. While the solution does not exhibit artifacts without a zero-slip boundary condition (e.g., no spurious large slip at the distant edges of the fault model), the latter helps ensure a well-behaved asymptotic decay of slip away from the source region. We also applied a soft zero-slip boundary condition at some segments of the fault trace at the surface where the data do not show a displacement discontinuity (e.g., on the eastern branch of the M7.1 rupture just south of the epicenter). This helps prevent a spurious shallow slip due to smoothness constraints on the slip distribution and relatively sparse sub-sampled points, as the displacement gradients across a "blind" fault trace may be relatively small (e.g., Wang and Fialko, 2015). The optimal values of the smoothness parameters and the relative weighting of different data sets (Sentinel-1, ALOS-2, Cosmo-Skymed, continuous and campaign GNSS) used in the inversion were determined using the Chi-Squared statistics (see figure S1 in the Supplemental Materials). We point out that while the regularization using smoothness constraints may appear as a somewhat arbitrary mathematical cure to the ill-conditioned nature of inverse problems, it does serve a purpose of discriminating against solutions that violate physical constraints such as the finite fault strength. Under a typical set of assumptions about the data and the model parameters, a Tikhonov-type regularization yields results that are similar to those obtained using the Bayesian inference methods that are however much more computationally expensive (e.g., Bishop, 1995; Vogel, 2002).

We performed two sets of inversions, one using Green's functions for a homogeneous elastic halfspace (Okada, 1985), and another for a layered elastic halfspace (Wang et al., 2003). For the latter, we computed elastic moduli from the three-dimensional (3-D) seismic tomography models of the Ridgecrest area (Hauksson and Unruh, 2007; Zhang and Lin, 2014). While the data in principle allow one to compute Green's functions for an elastic halfspace with a 3-D distribution of elastic moduli (e.g., Barbot et al., 2009b), the predicted deformation due to fault slip is mostly sensitive to variations in the elastic moduli with depth, as variations in the lateral direction are relatively minor. The average 1-D elastic rigidity structure used in our models is shown in Figure 5. For the sake of consistency, we adopted the same fault geometry in the homogeneous and layered halfspace models. In case of the layered models, rectangular fault patches were approximated by a superposition of point sources.

In addition to solving for the slip distribution given the assumed fault geometry, we performed inversions using a grid search in which the dip angles of various fault segments were allowed to vary. Results of these inversions are presented in the Supple-

mental Materials (Figures S2, S5), and in general lend support to the fault geometry constrained by the aftershock data (Figure 4).

Best-fit models: Results

Figure 6 shows the sub-sampled data points, predictions of the best-fit models, and residuals (the difference between the data and the model predictions) for the Sentinel-1 interferograms from the ascending and descending tracks. We compute residuals at the original (unsampled) resolution to illustrate the model fit to all of the data points, including those that were not used in the inversion. Overall, the model fits the main features of the displacement field quite well, with the variance reduction of more than 94%. Most of the misfit is concentrated near the rupture trace, where the assumption of elastic deformation off of the fault plane is likely violated (e.g., Kaneko and Fialko, 2011). Figure 7 shows the model fit to the Sentinel-1 range offsets. Model fits to the ALOS-2 and Cosmo-Skymed data are presented in Supplemental Materials (figures S6-S7). A comparison with other proposed models of the Ridgecrest earthquakes shows that our model is able to explain the data reasonably well (Wang et al., 2020).

Figure 8 shows the observed and modeled horizontal displacements at the continuous and campaign GNSS sites. We find that models that provide a good fit to the SAR data (provided the latter are available from a diverse set of look angles) are able to accurately "postdict" the independent GNSS data. The GNSS data therefore do not need to be heavily weighted in the joint inversions. The GNSS data are however quite useful for estimating and removing the long-wavelength trends and the "zero displacement" uncertainty in the LOS displacements, as discussed in section "SAR data". As one can see in Figure 8, our best-fit model renders a good agreement with the GNSS data, particularly in case of cGNSS (Figure 8a). For the campaign data, the fit is also adequate for sites that experienced large coseismic displacements. Sites with small displacements (and thus reduced SNR) render a poorer fit, in particular because many of the sites had the most recent occupation 15-20 years ago, so there is a large uncertainty in extrapolating the pre-seismic velocity (Floyd et al., 2020). Cyan triangles in Figure 8b denote campaign sites at which data were collected shortly after the July 2019 events, but not included in the inversion. In particular, we excluded sites at which the angle between the observed and modeled horizontal displacements exceeded 45° (GS04, GS25), or the magnitude of the observed and modeled horizontal displacements differed by more than a factor of two (GS16). For site GS20, no coseismic solution is available as the early post-earthquake data were corrupted because of a receiver malfunction.

Figures 9 and 10 show the slip distribution for the best-fit models assuming the homogeneous and layered elastic half-space, respectively. As expected, the slip distributions look similar; the main difference is that the slip is somewhat shallower and on average smaller in case of a homogeneous half-space compared to a layered half-space (e.g., Fialko, 2004). Tests using synthetic data indicate that the model resolution is not strongly dependent on depth (see Supplemental Figure S9).

We evaluate the "geodetic" moment magnitude $M_g = 2/3(\log_{10} GP - 9.1)$, where $G = 33$ GPa is the nominal shear modulus, and P is the seismic potency, computed as an algebraic sum $\Sigma_{i=1}^{N} A_i S_i$, where N is the number of slip patches (dislocations), and A_i and S_i are the area of, and the amplitude of slip on, patch i. Our models (Figures 9

and 10) correspond to a composite event consisting of the foreshock and the mainshock. Assuming that the foreshock was dominated by slip on the left-lateral faults 6 and 7, and the mainshock was dominated by slip on the right-lateral faults 1-5 (see Figure 4 for the segment numbers), we estimate M_g of 6.42 for the foreshock, and 7.03 for the mainshock in case of the homogeneous half-space model. In case of the layered half-space model, the respective values of the geodetic moment magnitude are 6.46, and 7.10. Thus the geodetic moments inferred from inversions of static displacements are in a good agreement with the seismic moments derived from the waveform spectra (see Data and Resources Section in the Supplemental Materials). This is similar to findings from previous studies of large events for which high-quality data are available (e.g., Barbot et al., 2009a; 2008b; Fialko, 2004; Fialko et al., 2005b; Simons et al., 2002; Wang and Fialko, 2018). In addition to providing a better agreement with the seismic data, more complex (and presumably more realistic) layered models appear to be more consistent with certain features of the geodetic data. While the homogeneous and layered half-space models on average fit the geodetic data equally well, we find that the layered models do a better job fitting the far-field decay of the coseismic displacements (Figure S8).

Apart from cross-faults that persist throughout the seismogenic layer (Ross et al., 2019), the M7.1 rupture appears to be geometrically simpler at depth than near the surface, where it branches out into splay faults of variable dip and strike. Accurately located aftershocks indicate a fairly linear rupture that strikes $\sim 320°$ (Figure 4a), with a gentle "helix-like" rotation from the westward dip in the north, to the eastward dip in the south (Figure 4b). In contrast, geodetically and geologically mapped fault trace exhibits deviations from the main trend illuminated by aftershocks, both along strike and down dip. In particular, the fault trace is shifted to the west with respect to the aftershock cloud in the central part of the rupture (Figure 4a), where the largest slip is inferred from the inversion (Figures 9 and 10). The shift is larger than that estimated by projecting the steeply dipping aftershock lineations to the surface. We interpret these observations as indicating a "Y-shaped" rupture geometry in the top few kilometers of the crust (Figure 4b), such that the main fault strand splits into two (or more) splay faults with variable dip angles above the depth of 3-4 km. A similar structure is also present to the north of the epicenter, where the two conjugate faults dipping toward each other form a mini-graben, with subsidence in between the faults, (see Figure 7a, around (-15,35) km in local coordinates), which requires a dip-slip component on the shallow splay faults (Figures 9 and 10). We refer to this preferred model as "Model A". We point out that the rather detailed inferences about the sub-surface fault geometry result from a joint analysis of precise seismic, geodetic, and geologic data, and would not be possible from consideration of individual data sets. For example, the aftershock data alone would be insufficient to reveal the details of the rupture geometry in the uppermost crust which is largely aseismic, and the geodetic and geologic data alone would be insufficient to detect changes in the fault dip angle with depth (Figure 4). For the sake of completeness, we also considered an alternative fault geometry in which the central part of the earthquake rupture consists of two sub-parallel sub-vertical non-intersecting faults. The respective model (Model B) is presented in the Supplementary Materials (Figures S10 and S11). While a sub-vertical western branch results in a somewhat better fit to the data on the western side of the fault, it would imply that the respective rupture segment is essentially devoid of aftershocks throughout the seismogenic layer, which we deem unlikely.

Stress changes due to the M6.4 foreshock and possible triggering of the M7.1 mainshock

A close spatiotemporal correlation between the M6.4 foreshock and the mainshock is suggestive of a cause and effect relationship, and raises a question about possible triggering mechanisms. A number of models were considered to explain interaction between earthquakes, including static (Anderson and Johnson, 1999; Caskey and Wesnousky, 1997; Hardebeck et al., 1998; King et al., 1994; Ziv and Rubin, 2000) and quasi-static (Deng and Sykes, 1997; Jonsson et al., 2003; Pollitz and Sacks, 2002; Segall, 1989) stress transfer, triggering by dynamic stress changes (Bellardinelli et al., 1999; Felzer et al., 2002; Gomberg et al., 1997; Lomnitz, 1996; Tymofyeyeva et al., 2019), etc. The 2019 Ridgecrest sequence offers a great opportunity to test the proposed models, not only because it was exceptionally well recorded, but also because it has a history of perturbations by nearby seismic events, in which only the most recent perturbation(s) of July 2019 culminated in a major earthquake.

While our finite fault model corresponds to a combination of the M6.4 foreshock and the mainshock, a good agreement between the geodetic moments computed for the left- and right-lateral faults, on the one hand, with the seismic moments of the foreshock and the mainshock, on the other hand, suggests that the seismic moment release due to the M6.4 foreshock was dominated by slip on the left-lateral NE-striking faults (segments 6 and 7 in Figure 4a). This in turn suggests that the foreshock involved relatively minor coseismic slip on a right-lateral NW-trending fault revealed by the aftershock activity following the M6.4 event (Chen et al., 2020; Ross et al., 2019). We verify this inference by comparing surface displacements due to the left-lateral faults from our best-fitting slip model to the GNSS observations of coseismic offsets due to the M6.4 event (Floyd et al., 2020). Figure S12 shows the model predictions (red arrows) and the observed horizontal displacements (blue arrows) from the continuous (white dots) and campaign (yellow triangles) GNSS sites. The data and the model predictions are in general agreement, including the high-fidelity cGNSS data. The fit to the campaign GNSS data is surprisingly good, considering that some of the sites have not been surveyed up to ~ 20 years prior to the 2019 earthquakes. While these results confirm that the moment release due to the M6.4 foreshock was dominated by slip on the left-lateral faults (approximated by segments 6 and 7 in our coseismic model, see Figure 4a), below we show that some amount of slip on the right-lateral NW-striking rupture is required to produce positive static Coulomb stress changes at the hypocenter of the M7.1 mainshock.

We ran several tests to see how much slip could have occurred on a right-lateral fault during the M6.4 foreshock. The model starts to notably over-predict the GNSS data if the magnitude of an equivalent event on a right-lateral fault exceeds 5.8 (which corresponds to ~ 0.4 m of average slip on a a NW-striking fault segment). Figure 11 shows the observed and modeled horizontal displacements due to the M6.4 foreshock involving slip on a system of high-angle antithetic strike-slip faults (denoted by green lines in Figure 11). We note that M5.8 is an upper bound on the equivalent amount of slip on the right-lateral fault. A larger moment release on the respective rupture segment would result in an over-prediction of both the surface displacements measured by the GNSS, and the scalar seismic moment (M6.4, see Data and Resources).

We used finite fault models derived for the M6.4 event to compute static stress changes at the hypocenter of the M7.1 mainshock. An important parameter in es-

timation of the induced stress changes is the orientation of a receiver fault. This is particularly relevant for the M7.1 Ridgecrest event given its complicated rupture geometry. In previous studies (e.g., Barnhart et al., 2019) static stress changes at the hypocenter of the July 5 mainshock were computed assuming that the earthquake rupture at depth follows the strike of the fault trace at the Earth surface. However, a comparison of the geometry of precisely relocated aftershocks and the fault trace show that the two are not necessarily correlated, as discussed in the previous section. Therefore we performed calculations for a range of possible fault orientations (see Data and Resources). Unless noted otherwise, all stress calculations presented below were performed using layered elastic half-space models assuming a rigidity structure shown in Figure 5. Figures 12a-c show stress perturbations due to slip on the left-lateral fault segments 6 and 7 (see Figures 4 and 11) resolved on vertical planes striking 320°, coincident with the overall trend of aftershocks of the M7.1 rupture (Figures 4). Stresses were computed at the hypocenter depth of the M7.1 event. Estimates of the hypocenter depth vary between 2 and 8 km below the mean sea level, depending on a method used (Hauksson and Jones, 2020). In our calculations we assume the depth of 7 km, accounting for the local elevation, and close to the values suggested by the full waveform inversions, as most reliable (Hauksson and Jones, 2020). Numerical tests show that the computed stress changes are not strongly dependent on the assumed depth of the hypocenter of the M7.1 event.

As one can see from Figures 12a-c, both shear and normal stress changes caused by slip on the left-lateral faults involved in the M6.4 foreshock at the hypocenter of the M7.1 rupture are close to zero, assuming that the mainshock nucleated on a slip plane aligned with the general trend of the M7.1 rupture (Figures 4). The computed Coulomb stress change is negligible compared to the negative Coulomb stress change due to a pair of M5+ earthquakes that occurred in 1995 (Hauksson et al., 1995) in the immediate vicinity of the hypocenter of the 2019 M7.1 event (Figure 12d-f, also see Figures S15 and S16 in the Supplemental Materials). A more northerly fault strike of 340°, consistent with a focal mechanism derived from the P-wave arrivals (see Data and Resources Section), provides for a more favorable orientation (Figure 12i), but the resolved Coulomb stress is still negative or close to zero. These calculations show that slip on the left-lateral faults that dominated the moment release from the M6.4 foreshock had a nearly neutral effect on the nucleation of the mainshock, and was certainly insufficient to overcome the stress shadow cast by the 1995 events. Allowing for a right-lateral slip on the NW-striking fault with an equivalent moment magnitude of 5.8 results in the positive Coulomb stress changes at the mainshock hypocenter (Figure 12l). Our calculations indicate that if the M7.1 event was triggered by static stress transfer due to foreshocks, the triggering was due to slip on the same right-lateral fault that was subsequently ruptured by the mainshock.

We also investigated the role of the second largest foreshock, the M5.4 event that occurred just hours before, and a few kilometers away from the hypocenter of the mainshock. An earlier study by Barnhart et al. (2019) assumed that the M5.4 event occurred on a NW-trending right-lateral fault, and estimated a positive Coulomb stress change of ~ 70 kPa at the hypocenter of the M7.1 event. However, detailed seismic studies showed that the M5.4 aftershock occurred on a left-lateral NE-trending fault (e.g., Shelly, 2020). Given a relatively small size of the foreshock, we generated a finite fault model assuming a circular rupture with a Gaussian slip distribution, subject to a constraint that the geodetic moment equals the seismic moment. The rupture

centroid and the effective radius were chosen such that most of the precisely located aftershocks of the M5.4 event occur on a periphery of the assumed slip distribution, as expected from the stress concentration arguments (e.g., Fialko, 2015). The calculated Coulomb stress changes at the mainshock hypocenter were found to be negative. However, sensitivity tests showed that the results are quite dependent on the assumed position of the centroid of the M5.4 rupture, because of its close proximity to the mainshock hypocenter. In particular, perturbing the along-strike centroid location by 2 km (likely within the uncertainties of the assumed slip distribution) affects the sign of the cumulative Coulomb stress change due to the 1995-2019 pre-mainshock sequence (Figure 13). Thus the answer to the question "was the nucleation of the M7.1 mainshock advanced by the cumulative static stress changes due to the nearby earthquakes" depends on details of slip models of the respective earthquakes, most notably the 2019 M5.4 foreshock, that are not well constrained by the available data. For values of the effective coefficient of friction that are higher than that assumed in calculations presented in this study (0.4), the predicted Coulomb stress changes are more negative, as the normal stress changes at the mainshock hypocenter are predominantly compressive (Figure 13b,e).

It is interesting to note that the hypocenter of the 2019 M7.1 event has experienced positive Coulomb stress changes due to shaking from the nearby events that were considerably (up to an order of magnitude) higher than the estimated static stress changes (see Figure S17 in the Supplemental Materials), yet the former failed to trigger a major earthquake at the time of shaking. This is evidence for the importance of quasi-static nucleation, rather than a critical yield stress, as the condition for triggering. Based on the results presented in this section, we conclude that the 2019 M7.1 mainshock nucleated on a fault oriented 340° (20 degrees west of north) that was likely nudged toward failure by the M6.4 foreshock, and subsequently either encouraged or discouraged by the M5.4 foreshock. Upon nucleating, the rupture propagated along a system of pre-existing faults on average striking 320°(40 degrees west of north). Activation of the pre-existing faults that were presumably less optimally oriented for failure with respect to the local stress field compared to the nucleation site could result from the onset of dynamic weakening (e.g., Brown and Fialko, 2012; Di Toro et al., 2011; Reches and Lockner, 2010; Rice, 2006).

Discussion

The 2019 M7.1 Ridgecrest earthquake shares a lot of similarities with the previous major earthquake that occurred in the Eastern California Shear Zone, the 1999 Hector Mine event (Figure 14). Both events nucleated on a fault strand striking at a larger angle compared to the average strike of the whole rupture. In case of the Hector Mine event, the fault strike correlates with topography (Fialko et al., 2005a); however, no such correlation exists in case of the Ridgecrest event, so that stresses due to topography cannot explain different orientations of the nucleation sites. A more likely explanation is that both earthquakes nucleated on a local structure that was more favorably oriented with respect to the regional stress field, and proceeded to rupture pre-existing faults that have been rotated away from an optimal orientation over time (e.g., by simple shear). If so, the rupture process may have involved dynamic triggering and weakening of the pre-existing faults.

Both the Ridgecrest and the Hector Mine ruptures exemplify complexity of immature developing strike-slip fault zones, with multiple sub-parallel branches and along-strike variations in the dip angle. Coseismic slip on closely spaced sub-parallel fault strands is puzzling, as dynamic rupture on a given fault interface is expected to discourage slip on nearby potential slip interfaces. More sophisticated dynamic rupture models are needed to better understand observations of slip on multiple sub-parallel fault strands. Finally, for both the Ridgecrest and the Hector Mine events, some of the fault strands broke the surface, while other strands remained blind and could only be detected with the help of precisely located aftershocks.

Among the main differences between the two events are the abundant cross-faults and shallow splay faults in case of the Ridgecrest earthquake. In part this difference could be attributed to regional variations in the stress regime. The Ridgecrest earthquakes occurred in a transtensional domain with concurrent strike-slip and normal faulting, as evidenced by e.g. the 1995 earthquake sequence that involved a pair of closely spaced strike-slip and normal faults (Hauksson et al., 1995, also, see Supplemental Materials, Figures S13 and S14). The shallow splay faults inferred from our inversions have dip angles around 60-70°, close to optimal orientation for normal faults. We interpret them as normal faults activated to accommodate a combination of the right-lateral slip and extension across the ECSZ. The geometry of our best-fit models in the shallow crust closely resembles the so-called "flower structures" recognized on a number of strike-slip faults world-wide (Bayasgalan et al., 1999; Harding, 1985; Sylvester, 1988).

It is of interest to evaluate how the coseismic slip amplitude varies with depth. Previous studies have suggested that for a number of M$\sim$ 7 strike-slip earthquakes the amount of slip in the middle of the seismogenic layer systematically exceeds the amount of slip at the surface (Fialko et al., 2005b; Hussain et al., 2016; Wang et al., 2014). While such behavior would be entirely expected for faults cutting through the velocity-strengthening layer in the top few kilometers of the Earth's crust (Hudnut and Sieh, 1989; Johnson et al., 2006; Marone and Scholz, 1988), where the coseismic slip is inhibited and most of slip occurs aseismically, for many faults that exhibit a larger coseismic slip at depth there is no evidence that aseismic slip is present and/or sufficiently robust to balance the slip budget. Such behavior, known as the shallow slip deficit (SSD), could be attributed to a number of mechanisms, including the presence of a soft damage zone (Barbot et al., 2008a), and dynamic damage due to propagating rupture fronts (Kaneko and Fialko, 2011; Roten et al., 2017). Inversions of high-quality geodetic data also show that a number of large strike-slip (or mixed mode) earthquakes are not associated with the SSD, although such events tend to be on a high end of the M7-M8 range (e.g., Tong et al., 2010; Zinke et al., 2014), possibly indicating differences between rupture styles on mature and immature faults.

Figure 15a shows a normalized distribution of slip as a function of depth for the M7.1 Ridgecrest earthquake (black solid line) obtained from our best-fitting model for a layered half-space (Figure 10), as well as for a number of other strike-slip earthquakes of comparable size for which high-quality geodetic data are available (color dashed lines). As one can see from Figure 15a, the maximum average slip due to the mainshock of the Ridgecrest sequence occurred in the depth interval between 3-4 km, essentially the same as inferred for other major strike-slip earthquakes analyzed using a consistent methodology. The estimated amount of the SSD is on the order of 30%, although the amplitude obviously depends on the degree of smoothing, with greater smoothing

resulting in smaller variations in the slip amplitude with depth. It is interesting to note that the inferred peak in the seismic moment release for system-size earthquakes that rupture the entire seismogenic layer (Figure 15a) is also apparent in the depth distribution of small earthquakes. Figure 15b shows the depth distribution of all of seismicity in California, as well as the aftershocks of the 2019 Ridgecrest earthquakes (see Data and Resources Section). We culled the earthquake catalogs to exclude events that have an absolute depth error greater than 1 km, and assigned the data to 1 km depth bins. The resulting data set consisting of $\sim 10^6$ events has a maximum in the mid-upper seismogenic zone, approximately in the same depth interval as the peak in the coseismic moment release by large earthquakes (Figure 15a). This is in contrast with models that predict that the most favorable conditions for the earthquake occurrence are met at the bottom of the seismogenic zone (Jiang and Fialko, 2016; Jiang and Lapusta, 2016; Sibson, 1982). Given the average thickness of the seismogenic layer in the continental crust on the order of 12-14km (e.g., Wright et al., 2013), results shown in Figure 15 suggest that the depth interval most conducive to unstable slip is in the upper part of the seismogenic zone. Catalogs of precisely located earthquakes with low magnitude of completeness from other seismically active regions are needed to test whether a similar depth dependence of "seismogenic potential" exists elsewhere.

Conclusions

The M7.1 July 5 2019 Ridgecrest earthquake was the largest earthquake in southern California since the 1999 Hector Mine earthquake, with which it shared a number of similarities. The Ridgecrest earthquake is characterized by a complex rupture geometry involving sub-parallel fault strands, along-strike variations in the dip angle, and shallow variations in the fault strike. The maximum slip occurred on shallow splay faults that were likely re-activated normal faults forming a classic "flower structure" on top of a reasonably straight right-lateral strike-slip fault at depth. Nucleation of unstable slip at the hypocenter of the M7.1 mainshock was discouraged by the pair of the M5+ events that occurred in the immediate vicinity of the hypocenter in August-September of 1995, only weakly if at all affected by slip on a left-lateral branch of the M6.4 foreshock, encouraged by slip on a right-lateral branch of the M6.4 foreshock, and likely discouraged by the M5.4 foreshock that occurred hours before the mainshock. Static stress changes near the hypocenter resolved on a mean trend of the M7.1 rupture were less favorable for failure compared to stress changes resolved on a more northerly striking fault plane indicated by the first motion data. This suggests that the M7.1 mainshock may have been triggered by the M6.4 foreshock on a slip patch that was optimally oriented for failure with respect to the local stress field, and subsequently triggered unstable slip on a less favorably oriented pre-existing right-lateral fault system. Dynamic stress changes from the nearby earthquakes failed to trigger the mainshock, despite the fact that they were much larger than any static stress change that might have advanced the nucleation of unstable slip. Slip models derived from inversions of surface deformation data reveal a moderate amount of shallow slip deficit. Subsequent studies of postseismic deformation will show if the inferred amount of the co-seismic slip deficit can be accommodated by means of creep in the uppermost crust. The estimated depth of the maximum slip averaged along the rupture length is 3-4 km, similar to results from previous studies of major strike-slip earthquakes, and to

the depth distribution of precisely located seismicity in California, suggesting that the respective depth interval maximizes a potential for seismic instabilities.

Acknowledgments

References

Ahmed, R., P. Siqueira, S. Hensley, B. Chapman, and K. Bergen (2011). A survey of temporal decorrelation from spaceborne L-Band repeat-pass InSAR, *Remote Sensing of Environment*, **115** 2887–2896.

Anderson, G. and H. Johnson (1999). A new statistical test for static stress triggering: Application to the 1987 Superstition Hills earthquake sequence, *J. Geophys. Res.*, **104** 20153–20168.

Barbot, S., Y. Fialko, and Y. Bock (2009a). Postseismic deformation due to the Mw 6.0 2004 Parkfield earthquake: Stress-driven creep on a fault with spatially variable rate-and-state friction parameters, *J. Geophys. Res.*, **114** B07405.

Barbot, S., Y. Fialko, and D. Sandwell (2008a). Effect of a compliant fault zone on the inferred earthquake slip distribution, *J. Geophys. Res.*, **113** B06404, doi:10.1029/2007JB005256.

Barbot, S., Y. Fialko, and D. Sandwell (2009b). Three-dimensional models of elastostatic deformation in heterogeneous media, with applications to the Eastern California Shear Zone, *Geophys. J. Int.*, **179** 500–520.

Barbot, S., Y. Hamiel, and Y. Fialko (2008b). Space geodetic investigation of the co- and post-seismic deformation due to the 2003 M_w 7.1 Altai earthquake: Implications for the local lithospheric rheology, *J. Geophys. Res.*, **113** B03403.

Barnhart, W. D., G. P. Hayes, and R. D. Gold (2019). The July 2019 Ridgecrest, California, earthquake sequence: Kinematics of slip and stressing in cross-fault ruptures, *Geophys. Res. Lett.*, **46** 11859–11867.

Bayasgalan, A., J. Jackson, J.-F. Ritz, and S. Carretier (1999). Forebergs', flower structures, and the development of large intra-continental strike-slip faults: the Gurvan Bogd fault system in Mongolia, *J. Struct. Geol.*, **21** 1285–1302.

Bellardinelli, M. E., M. Cocco, O. Coutant, and F. Cotton (1999). Redistribution of dynamic stress during coseismic ruptures: Evidence for fault interaction and earthquake triggering, *J. Geophys. Res.*, **104** 14925–14945.

Bishop, C. M. (1995). Training with noise is equivalent to Tikhonov regularization, *Neural computation*, **7** 108–116.

Brown, K. M. and Y. Fialko (2012). "Melt welt" mechanism of extreme weakening of gabbro at seismic slip rates, *Nature*, **488** 638–641.

Caskey, S. J. and S. G. Wesnousky (1997). Static stress change and earthquake triggering during the 1954 Fairview Peak and Dixie Valley earthquakes, Central Nevada, *Bull. Seism. Soc. Am.*, **87** 521–527.

Chen, K., J.-P. Avouac, S. Aati, C. Milliner, F. Zheng, and C. Shi (2020). Cascading and pulse-like ruptures during the 2019 Ridgecrest earthquakes in the Eastern California Shear Zone, *Nature Communications*, **11** 1–8.

Deng, J. and L. R. Sykes (1997). Evolution of the stress field in Southern California and triggering of moderate-size earthquakes: A 200-year perspective, *J. Geophys. Res.*, **102** 9859–9886.

Di Toro, G., R. Han, T. Hirose, N. De Paola, S. Nielsen, K. Mizoguchi, F. Ferri, M. Cocco, and T. Shimamoto (2011). Fault lubrication during earthquakes, *Nature*, **471** 494–498.

Dokka, R. K. and C. J. Travis (1990). Role of the Eastern California shear zone in accommodating Pacific-North American plate motion, *Geophys. Res. Lett.*, **17** 1323–1327.

Farr, T. and M. Kobrick (2000). Shuttle Radar Topography Mission produces a wealth of data, *AGU Eos*, **81** 583–585.

Felzer, K. R., T. W. Becker, R. E. Abercrombie, G. Ekström, and J. R. Rice (2002). Triggering of the 1999 Mw 7.1 Hector Mine earthquake by aftershocks of the 1992 Mw 7.3 Landers earthquake, *J. Geophys. Res.*, **107** ESE–6.

Fialko, Y. (2004). Probing the mechanical properties of seismically active crust with space geodesy: Study of the co-seismic deformation due to the 1992 M_w7.3 Landers (southern California) earthquake, *J. Geophys. Res.*, **109** B03307, 10.1029/2003JB002756.

Fialko, Y. (2015), Fracture and Frictional Mechanics - Theory, In Schubert, G., editor, *Treatise on Geophysics, 2nd. Ed., Vol. 4*, pages 73–91. Elsevier Ltd., Oxford.

Fialko, Y., Z. Jin, E. Tymofyeyeva, and M. A. Floyd (2019a), Ridgecrest California Earthquake Post-Event Response July 2019 UCSD, doi:10.7283/YJK0-B215, Technical report, UNAVCO, Inc., GPS/GNSS Observations Dataset.

Fialko, Y., Z. Jin, E. Tymofyeyeva, D. T. Sandwell, J. Haase, and M. A. Floyd (2019b), Ridgecrest California Earthquake Response July 2019 UCSD, doi:10.7283/N74Q-GA66, Technical report, UNAVCO, Inc., GPS/GNSS Observations Dataset.

Fialko, Y., L. Rivera, and H. Kanamori (2005a). Estimate of differential stress in the upper crust from variations in topography and strike along the San Andreas fault, *Geophys. J. Int.*, **160** 527–532.

Fialko, Y., D. Sandwell, M. Simons, and P. Rosen (2005b). Three-dimensional deformation caused by the Bam, Iran, earthquake and the origin of shallow slip deficit, *Nature*, **435** 295–299.

Fialko, Y., M. Simons, and D. Agnew (2001). The complete (3-D) surface displacement field in the epicentral area of the 1999 M_w7.1 Hector Mine earthquake, southern California, from space geodetic observations, *Geophys. Res. Lett.*, **28** 3063–3066.

Floyd, M., G. Funning, Y. A. Fialko, R. L. Terry, and T. Herring (2020). Survey and Continuous GNSS in the vicinity of the July 2019 Ridgecrest earthquakes, in press, *Seismol. Res. Lett.*, **91**.

Goldstein, R. M., H. A. Zebker, and C. L. Werner (1988). Satellite radar interferometry: Two-dimensional phase unwrapping, *Radio science*, **23** 713–720.

Golub, G. H., P. C. Hansen, and D. P. O'Leary (1999). Tikhonov regularization and total least squares, *SIAM journal on matrix analysis and applications*, **21** 185–194.

Gomberg, J., M. L. Blanpied, and N. M. Beeler (1997). Transient triggering of near and distant earthquakes, *Bull. Seism. Soc. Am.*, **87** 294–309.

Gonzalez-Ortega, A., Y. Fialko, D. Sandwell, F. Alejandro Nava-Pichardo, J. Fletcher, J. Gonzalez-Garcia, B. Lipovsky, M. Floyd, and G. Funning (2014). El Mayor-Cucapah ($M_w7.2$) earthquake: Early near-field postseismic deformation from InSAR and GPS observations, *J. Geophys. Res.*, **119** 1482–1497.

Hardebeck, J. L., J. J. Nazareth, and E. Hauksson (1998). The static stress change triggering model: Constraints from two southern California aftershock sequences, *J. Geophys. Res.*, **103** 24427–24437.

Harding, T. P. (1985). Seismic characteristics and identification of negative flower structures, positive flower structures, and positive structural inversion, *AAPG Bulletin*, **69** 582–600.

Hauksson, E., K. Hutton, H. Kanamori, L. Jones, J. Mori, S. Hough, and G. Roquemore (1995). Preliminary report on the 1995 Ridgecrest earthquake sequence in eastern California, *Seismol. Res. Lett.*, **66** 54–60.

Hauksson, E. and L. Jones (2020). Seismicity, Stress State, and Style of Faulting of the Ridgecrest-Coso Region from the 1930s through 2019: Seismotectonics of an Evolving Plate boundary Segment, *Bull. Seism. Soc. Am.*, **XX**, submitted.

Hauksson, E., L. Jones, and K. Hutton (2002). The 1999 M_w 7.1 Hector Mine, California, earthquake sequence: Complex conjugate strike-slip faulting, *Bull. Seism. Soc. Am.*, **92** 1154–1170.

Hauksson, E., P. Small, K. Hafner, R. Busby, R. Clayton, J. Goltz, T. Heaton, K. Hutton, H. Kanamori, J. Polet, et al. (2001). Southern California seismic network: Caltech/USGS element of TriNet 1997-2001, *Seismol. Res. Lett.*, **72** 690–704.

Hauksson, E. and J. Unruh (2007). Regional tectonics of the Coso geothermal area along the intracontinental plate boundary in central eastern California: Three-dimensional V_p and V_p/V_s models, spatial-temporal seismicity patterns, and seismogenic deformation, *J. Geophys. Res.*, **112** B06309.

Herring, T. A., T. I. Melbourne, M. H. Murray, M. A. Floyd, W. M. Szeliga, R. W. King, D. A. Phillips, C. M. Puskas, M. Santillan, and L. Wang (2016). Plate Boundary Observatory and related networks: GPS data analysis methods and geodetic products, *Reviews of Geophysics*, **54** 759–808.

Hudnut, K. W. and K. E. Sieh (1989). Behavior of the Superstition Hills fault during the past 330 years, *Bull. Seism. Soc. Am.*, **79** 304–329.

Hussain, E., T. J. Wright, R. J. Walters, D. Bekaert, A. Hooper, and G. A. Houseman (2016). Geodetic observations of postseismic creep in the decade after the 1999 Izmit earthquake, Turkey: Implications for a shallow slip deficit, *J. Geophys. Res.*, **121** 2980–3001.

Jennings, C. and W. Bryant (2010), Fault Activity Map of California, California Division of Mines and Geology, Geologic Data Map No. 6.

Jiang, J. and Y. Fialko (2016). Reconciling seismicity and geodetic locking depths on the Anza section of the San Jacinto fault, *Geophys. Res. Lett.*, **43** 10663–10671.

Jiang, J. and N. Lapusta (2016). Deeper penetration of large earthquakes on seismically quiescent faults, *Science*, **352** 1293–1297.

Johnson, K. M., R. Bürgmann, and K. Larson (2006). Frictional properties on the San Andreas Fault near Parkfield, California, inferred from models of afterslip following the 2004 earthquake, *Bull. Seism. Soc. Am.*, **96** S321–S338.

Jonsson, S., P. Segall, R. Pedersen, and G. Bjornsson (2003). Post-earthquake ground movements correlated to pore-pressure transients, *Nature*, **424** 179–183.

Jonsson, S., H. Zebker, P. Segall, and F. Amelung (2002). Fault slip distribution of the 1999 M_w 7.1 Hector Mine, California, earthquake, estimated from satellite radar and GPS measurements, *Bull. Seism. Soc. Am.*, **92** 1377–1389.

Kaneko, Y. and Y. Fialko (2011). Shallow slip deficit due to large strike-slip earthquakes in dynamic rupture simulations with elasto-plastic off-fault response, *Geophys. J. Int.*, **186** 1389–1403.

King, G. C. P., R. S. Stein, and J. Lin (1994). Static stress changes and the triggering of earthquakes, *Bull. Seismol. Soc. Am.*, **84** 935–953.

Liu, C., T. Lay, E. E. Brodsky, K. Dascher-Cousineau, and X. Xiong (2019). Coseismic rupture process of the large 2019 Ridgecrest earthquakes from joint inversion of geodetic and seismological observations, *Geophys. Res. Lett.*, **46** 11820–11829.

Lomnitz, C. (1996). Search of a worldwide catalog for earthquakes triggered at intermediate distances, *Bull. Seism. Soc. Am.*, **86** 293–298.

Marone, C. and C. H. Scholz (1988). The depth of seismic faulting and the upper transition from stable to unstable slip regimes, *Geophys. Res. Lett.*, **15** 621–624.

McClusky, S., S. Bjornstad, B. Hager, R. King, B. Meade, M. Miller, F. Monastero, and B. Souter (2001). Present day kinematics of the Eastern California Shear Zone from a geodetically constrained block model, *Geophys. Res. Lett.*, **28** 3369–3372.

Mitchell, E., Y. Fialko, and K. M. Brown (2016). Velocity-weakening behavior of Westerly granite at temperature up to 600° C, *J. Geophys. Res.*, **121** 6932–6946.

Nur, A., H. Ron, and G. Beroza (1993). The nature of the Landers-Mojave earthquake line, *Science*, **261** 201–203.

Okada, Y. (1985). Surface deformations due to shear and tensile faults in a halfspace, *Bull. Seism. Soc. Am.*, **75** 1135–1154.

Pollitz, F. F. and I. S. Sacks (2002). Stress triggering of the 1999 Hector Mine earthquake by transient deformation following the 1992 Landers earthquake, *Bull. Seism. Soc. Am.*, **92** 1487–1496.

Ponti, D., J. L. Blair, C. Rosa, K. Thomas, A. Pickering, S. Akciz, S. Angster, J. Avouac, J. Bachhuber, S. Bacon, et al. (2020), Documentation of surface fault rupture and ground deformation features produced by the ridgecrest m6. 4 and m7. 1 earthquake sequence of july 4 and 5, 2019, in press.

Reches, Z. and D. A. Lockner (2010). Fault weakening and earthquake instability by powder lubrication, *Nature*, **467**.

Rice, J. R. (2006). Heating and weakening of faults during earthquake slip, *J. Geophys. Res.*, **111** B05311.

Rice, J. R. and S. T. Tse (1986). Dynamic motion of a single degree of freedom system following a rate and state dependent friction law, *J. Geophys. Res.*, **91** 521–530.

Ross, Z. E., B. Idini, Z. Jia, O. L. Stephenson, M. Zhong, X. Wang, Z. Zhan, M. Simons, E. J. Fielding, S.-H. Yun, et al. (2019). Hierarchical interlocked orthogonal faulting in the 2019 Ridgecrest earthquake sequence, *Science*, **366** 346–351.

Roten, D., K. Olsen, and S. Day (2017). Off-fault deformations and shallow slip deficit from dynamic rupture simulations with fault zone plasticity, *Geophys. Res. Lett.*, **44** 7733–7742.

Sandwell, D., R. Mellors, X. Tong, M. Wei, and P. Wessel (2011). Open radar interferometry software for mapping surface deformation, *Eos, Trans. AGU*, **92** 234–234.

Sauber, J., W. Thatcher, and S. Solomon (1986). Geodetic measurement of deformation in the central Mojave Desert, California, *J. Geophys. Res.*, **91** 2683–2693.

Segall, P. (1989). Earthquakes triggered by fluid extraction, *Geology*, **17** 942–946.

Shelly, D. R. (2020). A high-resolution seismic catalog for the initial 2019 Ridgecrest earthquake sequence: Foreshocks, aftershocks, and faulting complexity, *Seismol. Res. Lett.*, **91**.

Sibson, R. H. (1982). Fault zone models, heat flow, and the depth distribution of earthquakes in the continental crust of the united states, *Bulletin of the Seismological Society of America*, **72** 151–163.

Sieh, K., L. Jones, E. Hauksson, K. Hudnut, D. Eberhart-Phillips, T. Heaton, S. Hough, K. Hutton, H. Kanamori, A. Lilje, et al. (1993). Near-field investigations of the Landers earthquake sequence, *Science*, **260** 171–176.

Simons, M., Y. Fialko, and L. Rivera (2002). Coseismic deformation from the 1999 M_w7.1 Hector Mine, California, earthquake, as inferred from InSAR and GPS observations, *Bull. Seism. Soc. Am.*, **92** 1390–1402.

Sylvester, A. (1988). Strike-slip faults, *Geol. Soc. Am. Bull.*, **100** 1666–1703.

Tong, X., D. Sandwell, and Y. Fialko (2010). Coseismic slip model of the 2008 Wenchuan earthquake derived from joint inversion of interferometric synthetic aperture radar, GPS, and field data, *J. Geophys. Res.*, **115** B04314.

Tymofyeyeva, E. and Y. Fialko (2015). Mitigation of atmospheric phase delays in InSAR data, with application to the eastern California shear zone, *J. Geophys. Res.*, **120** 5952–5963, 2015JB011886.

Tymofyeyeva, E., Y. Fialko, J. Jiang, X. Xu, D. Sandwell, R. Bilham, T. K. Rockwell, C. Blanton, F. Burkett, A. Gontz, and S. Moafipoor (2019). Slow slip event on the southern San Andreas fault triggered by the 2017 M_w8.2 Chiapas (Mexico) earthquake, *J. Geophys. Res.*, **124** 9956–9975.

Vogel, C. R. (2002), *Computational methods for inverse problems*, volume 23, Society for Industrial and Applied Mathematics.

Wang, K., D. Dreger, E. Tinti, R. Bürgrmann, and T. Taira (2020), Rupture process of the 2019 Ridgecrest, California M6.4 foreshock and M7.1 earthquake constrained by seismic and geodetic Data, submitted.

Wang, K. and Y. Fialko (2014). Space geodetic observations and models of postseismic deformation due to the 2005 M7.6 Kashmir (Pakistan) earthquake, *J. Geophys. Res.*, **119** 7306–7318.

Wang, K. and Y. Fialko (2015). Slip model of the 2015 M_w 7.8 Gorkha (Nepal) earthquake from inversions of ALOS-2 and GPS data, *Geophys. Res. Lett.*, **42** 7452–7458.

Wang, K. and Y. Fialko (2018). Observations and modeling of co- and postseismic deformation due to the 2015 M_w 7.8 Gorkha (Nepal) earthquake, *J. Geophys. Res.*, **123** 761–779.

Wang, K., X. Xu, and Y. Fialko (2017). Improving burst alignment in TOPS interferometry with bivariate enhanced spectral diversity (BESD), *IEEE Geoscience and Remote Sensing Letters*, **14** 2423–2427.

Wang, R., F. Martin, and F. Roth (2003). Computation of deformation induced by earthquakes in a multi-layered elastic crust - FORTRAN programs ED-GRN/EDCMP, *Comp. Geosci.*, **29** 195–207.

Wang, Y., Y.-N. N. Lin, M. Simons, and S. T. Tun (2014). Shallow rupture of the 2011 Tarlay earthquake (Mw 6.8), eastern Myanmar, *Bull. Seism. Soc. Am.*, **104** 2904–2914.

Wessel, P., W. H. F. Smith, R. Scharroo, J. Luis, and F. Wobbe (2013). Generic Mapping Tools: Improved Version Released, *Eos, Trans. AGU*, **94** 409–410.

Wright, T. J., J. R. Elliott, H. Wang, and I. Ryder (2013). Earthquake cycle deformation and the Moho: Implications for the rheology of continental lithosphere, *Tectonophysics*, **609** 504–523.

Zhang, Q. and G. Lin (2014). Three-dimensional V_p and V_p/V_s models in the Coso geothermal area, California: Seismic characterization of the magmatic system, *J. Geophys. Res.*, **119** 4907–4922.

Zinke, R., J. Hollingsworth, and J. F. Dolan (2014). Surface slip and off-fault deformation patterns in the 2013 Mw7.7 Balochistan, Pakistan earthquake: Implications for controls on the distribution of near-surface coseismic slip, *Geochemistry, Geophysics, Geosystems*, **15** 5034–5050.

Ziv, A. and A. Rubin (2000). Static stress transfer and earthquake triggering: No lower threshold in sight?, *J. Geophys. Res.*, **105** 13631–13642.

List of Figure Captions

1. Regional map of the study area.

2. Surface Deformation observed using InSAR data.

3. Two examples of campaign GNSS sites.

4. Map view of seismicity distribution and locations of modeled fault segments.

5. Averaged 1-D elastic rigidity structure used in our models.

6. Sub-sampled data, best-fitting models, and residuals for the Sentinel-1 radar interferograms.

7. Sub-sampled data, best-fitting models, and residuals for the Sentinel-1 range offsets.

8. Observed and modeled horizontal coseismic displacements at the continuous and campaign GNSS sites.

9. Slip distribution from a homogeneous elastic half-space model.

10. Slip distribution from a layered elastic half-space model.

11. Observed and modeled horizontal coseismic displacements due to the M6.4 foreshock.

12. Static stress changes due to the pre-mainshock seismicity (not including the M5.4 foreshock).

13. Static stress changes due to the pre-mainshock seismicity (including the M5.4 foreshock).

14. A comparison of the 2019 Ridgecrest and the 1999 Hector Mine rupture traces.

15. Depth distribution of along-strike averaged coseismic slip for several M7 earthquakes, aftershocks of the 2019 Ridgecrest events, and all of seismicity in California.

Table 1: SAR data used in this study. Spatial coverage of each data set is shown in Figure 1.

Heading track number	Interferometric pairs	Time span (days)	Satellites	$B_\perp$ (m)
Descending 71	2019/07/04 - 2019/07/16	12	Sentinel-1	29.7
Descending 21	2019/06/27 - 2019/07/13	16	Cosmo-Skymed	176.2
Ascending 64	2019/07/04 - 2019/07/10	16	Sentinel-1	126.6
Ascending 14	2019/07/04 - 2019/07/20	16	Cosmo-Skymed	452.4
Ascending 65	2016/08/08 - 2019/07/08	1064	ALOS-2	2.4
Ascending 66	2017/08/12 - 2019/07/13	700	ALOS-2	14.6

[1] Smaller perpendicular baselines ($B_\perp$) and larger radar wavelengths result in a better correlation of the radar phase.

[2] The resolution of Sentinel-1 range offsets is 2.3m, and the resolution of Cosmo-Skymed azimuth offsets is 2.2m.
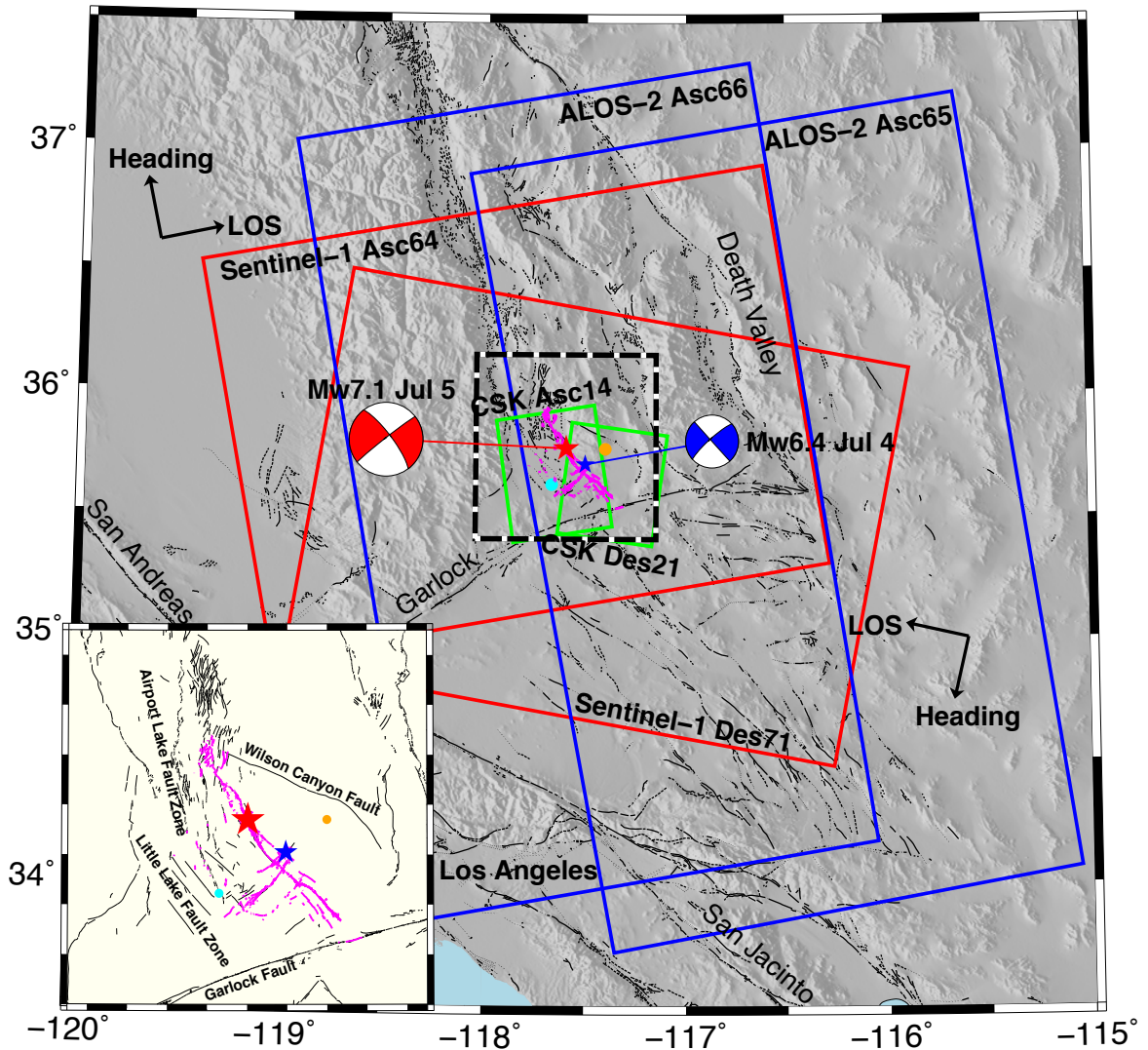
Figure 1: Regional map of the study area. Magenta lines denote surface offsets due to the Ridgecrest earthquakes mapped by field surveys (Ponti et al., 2020). Red and blue stars denote the epicenters of M7.1 and M6.4 earthquakes, and red and blue "beach balls" denote the respective focal mechanisms. The red, blue and green polygons represent swaths of Synthetic Aperture Radar (SAR) data from Sentinel-1, ALOS-2 and Cosmo-Skymed satellite missions used in this study. Arrows show the satellite heading (azimuth) and look (range) direction for the ascending and descending satellite orbits. Black wavy lines denote mapped active faults (Jennings and Bryant, 2010). The cyan and orange dots denote the towns of Ridgecrest and Searles Valley, respectively. The inset shows a close-up view of the earthquake area outlined by the dashed rectangle.
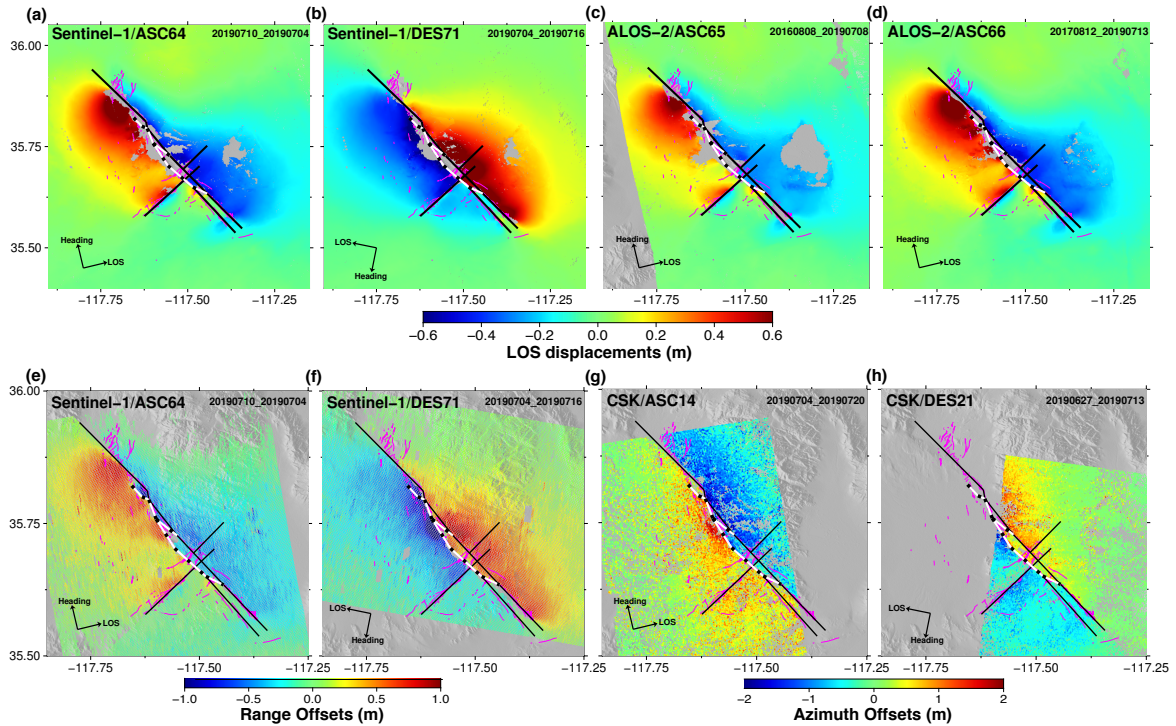
Figure 2: (a-d) LOS displacements from Sentinel-1 interferograms from the ascending (a) and descending (b) tracks, and ALOS-2 interferograms from two ascending tracks (c,d). (e-f) Range offsets from the Sentinel-1 data (same pairs as in panels a and b). (g-h) Azimuth offsets from the Cosmo-Skymed data. Positive LOS displacements correspond to motion toward the satellite. Black lines represent a piece-wise linear approximation of the rupture trace based on all available data (interferograms, range and azimuth offsets, seismicity, field data). Solid black lines denote sub-vertical faults that extend throughout the seismogenic layer, and dotted black and white lines denote surface traces of shallow splay faults. Magenta lines indicate rupture traces mapped by field surveys.
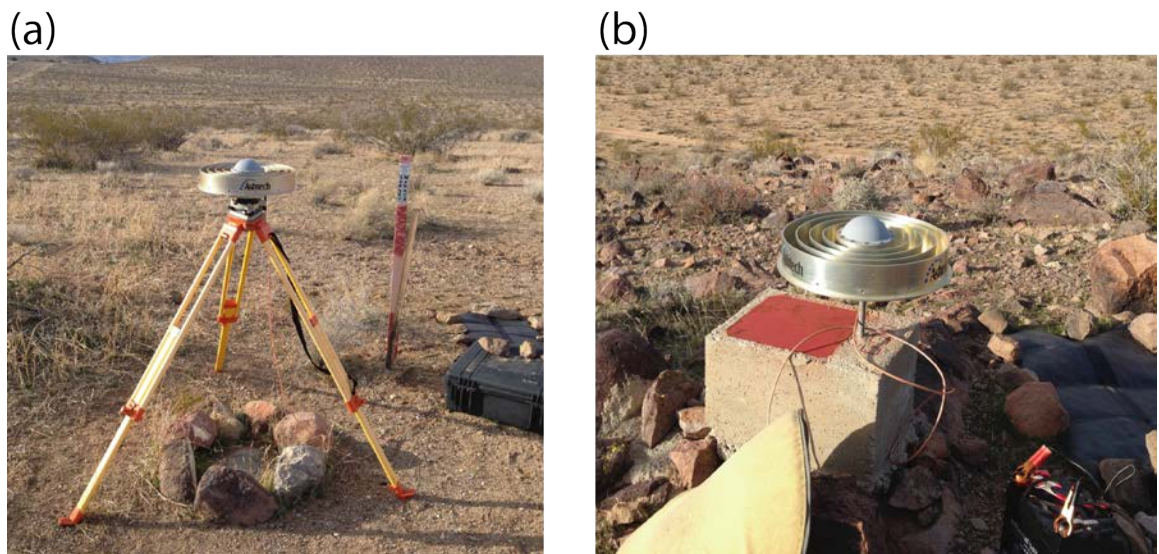
Figure 3: (a) Campaign site 0806. (b) Campaign site GS11.
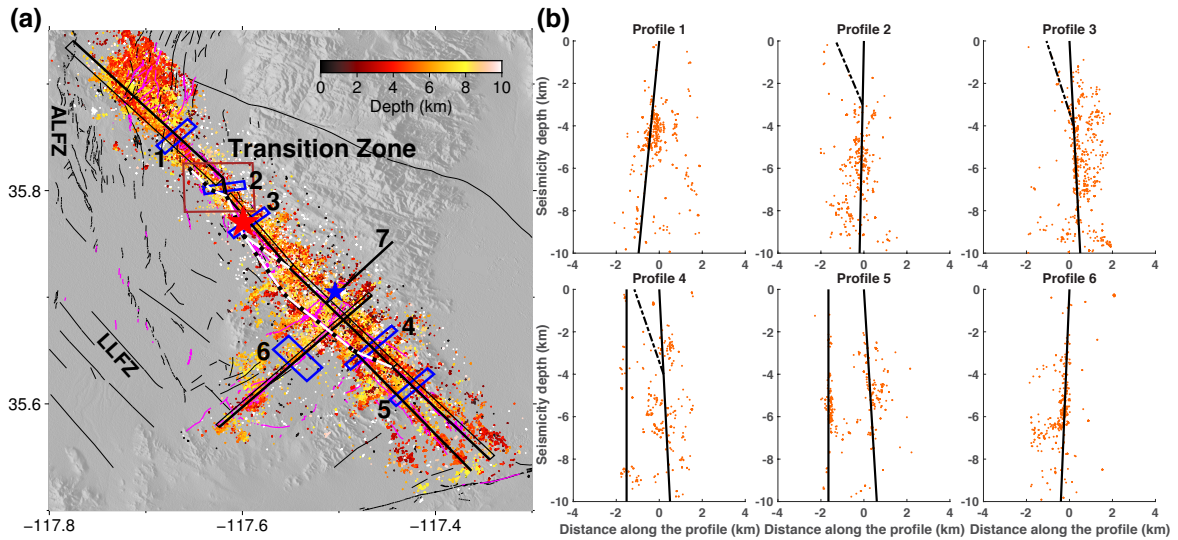
Figure 4: (a) Map view of aftershocks produced by the Ridgecrest events. Color dots represent the aftershock epicenters, color-coded by depth. Magenta lines represent surface traces of the 2019 earthquakes (Ponti et al., 2020), and black lines represent Quaternary faults (Jennings and Bryant, 2010). Solid and dotted black lines denote surface traces of modeled fault planes. Solid thin rectangles correspond to fault planes that extend to the bottom of the seismogenic zone, and dotted lines correspond to shallow splay faults. Epicenters of the M6.4 and M7.1 events are indicated by blue and red stars (same as in Figure 2). Blue rectangles correspond to the cross-section profiles shown in panel (b). Area of diffuse seismicity at the northern end of the M7.1 rupture is truncated at 5 km from the fault trace. LLFZ = Little Lake Fault Zone; ALFZ = Airport Lake Fault Zone. (b) Seismicity distribution and locations of the modeled fault segments in several cross sections across the fault trace; see the respective profiles in panel (a). Dashed lines denote the splay faults that connect surface offsets to seismicity that starts at depth of 3∼ 4 km. The downdip extent of aftershocks is ∼ 10 km.
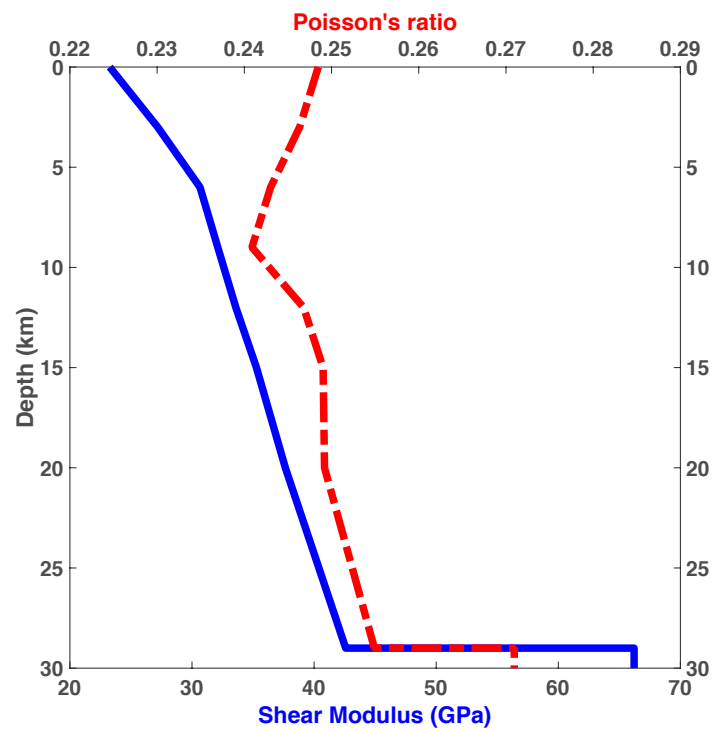
Figure 5: Variations in the elastic shear modulus (blue line, bottom axis) and Poisson's ratio (dashed red line, top axis) as a function of depth, as inferred from the seismic velocity model of Zhang and Lin (2014).
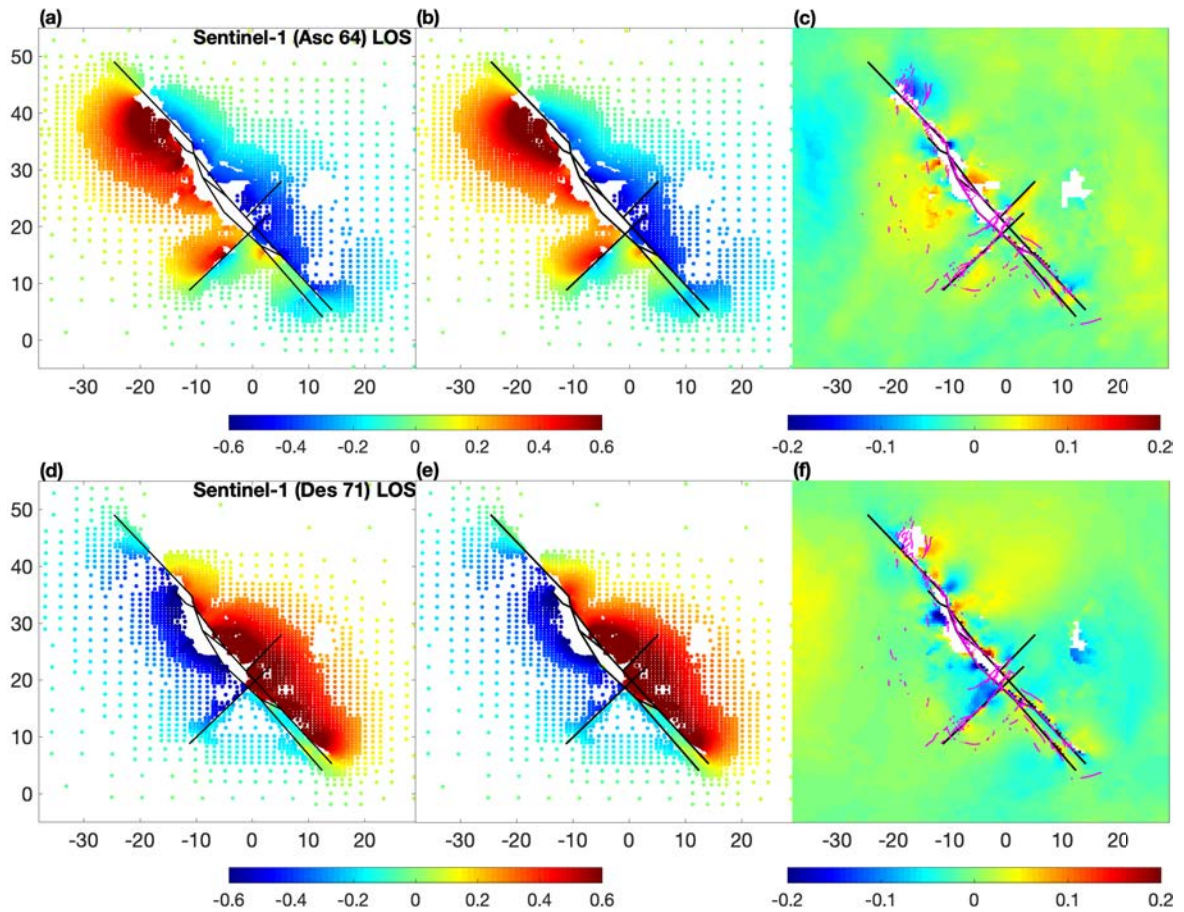
Figure 6: (a,d) Sub-sampled data, (b,e) best-fitting models, and (c,f) residuals for the Sentinel-1 radar interferograms from the ascending track 64 (a-c), and descending track 71 (d-f). Colors denote the amplitude of LOS displacements, in m. Motion toward the satellite is deemed positive. Horizontal and vertical axes are in UTM coordinates (eastings and northings, respectively), in km, with respect to a local origin (117.5°W, 35.5°N).
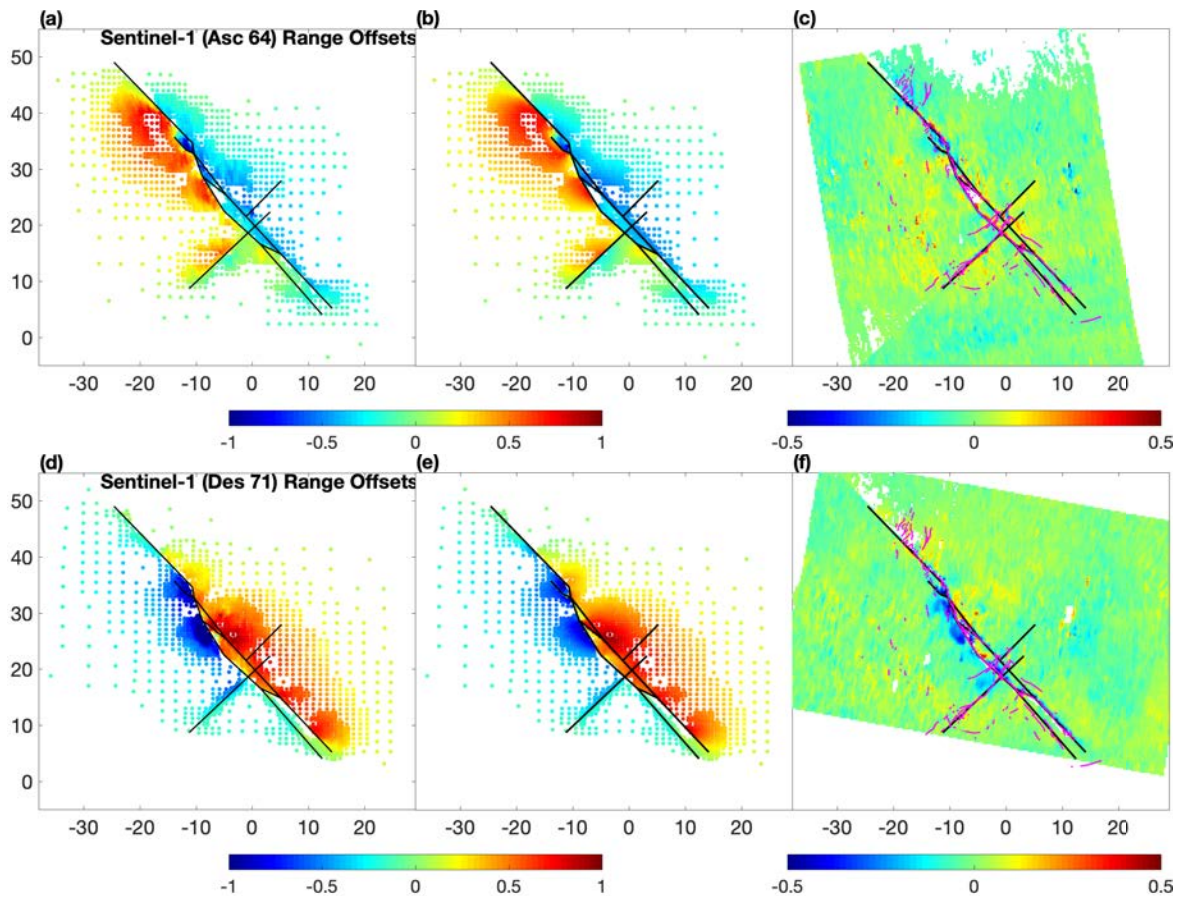
Figure 7: (a,d) Sub-sampled data, (b,e) best-fitting models, and (c,f) residuals for the Sentinel-1 range offsets from the ascending track 64 (a-c), and descending track 71 (d-f). Colors denote the amplitude of range offsets, in m. Other notation is the same as in Figure 6.
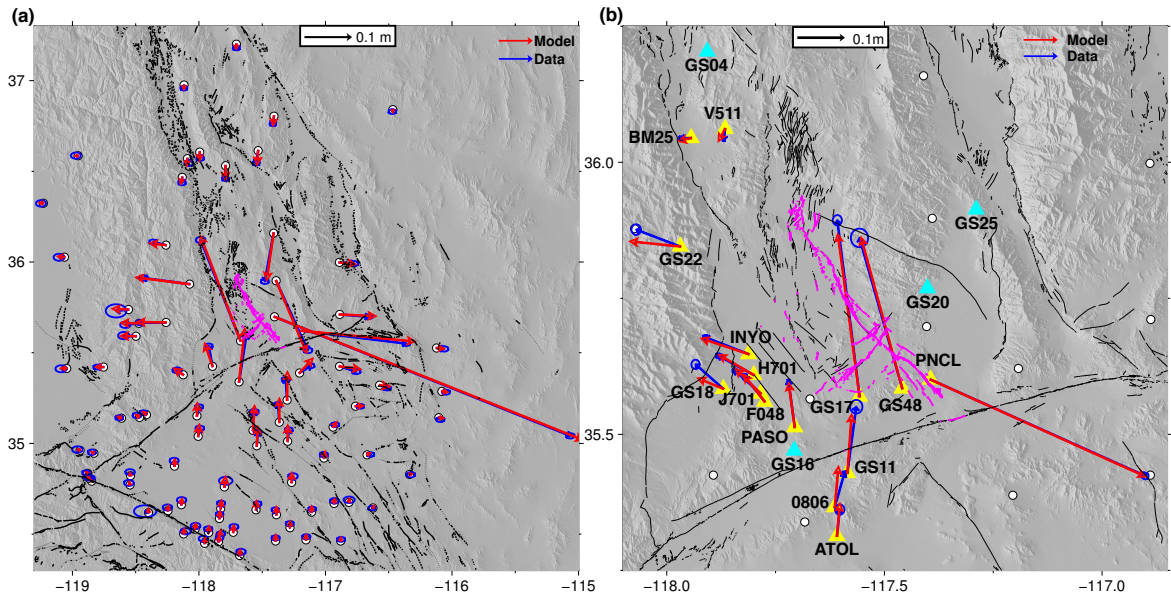
Figure 8: (a) Observed (blue arrows) and modeled (red arrows) horizontal coseismic displacements at the cGNSS sites (white circles) of the PBO network. The ellipses show the 2-sigma errors. (b) Same as in panel (a), for the campaign GNSS sites (yellow triangles). Cyan triangles denote campaign sites at which data was collected, but not used in the inversions due to quality issues. White circles denote the location of the cGNSS sites. Solutions for the coseismic offsets are from Floyd et al. (2020).
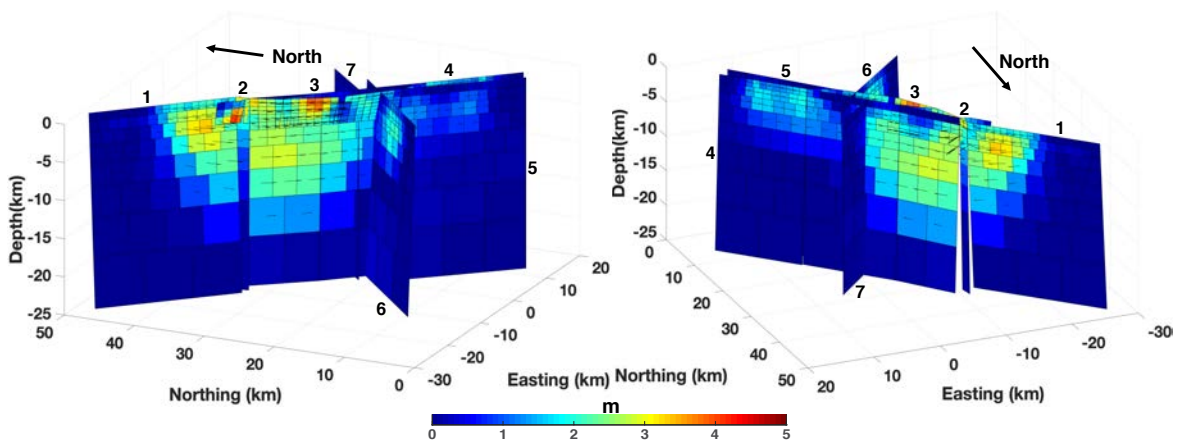
Figure 9: Slip distribution from the joint inversion of space geodetic data using a homogeneous elastic half-space model. Colors denote the total amplitude of slip, and arrows show the direction of slip. The two panels represent perspectives from different vantage points. The calculated geodetic moment magnitude for the mainshock is M7.03.
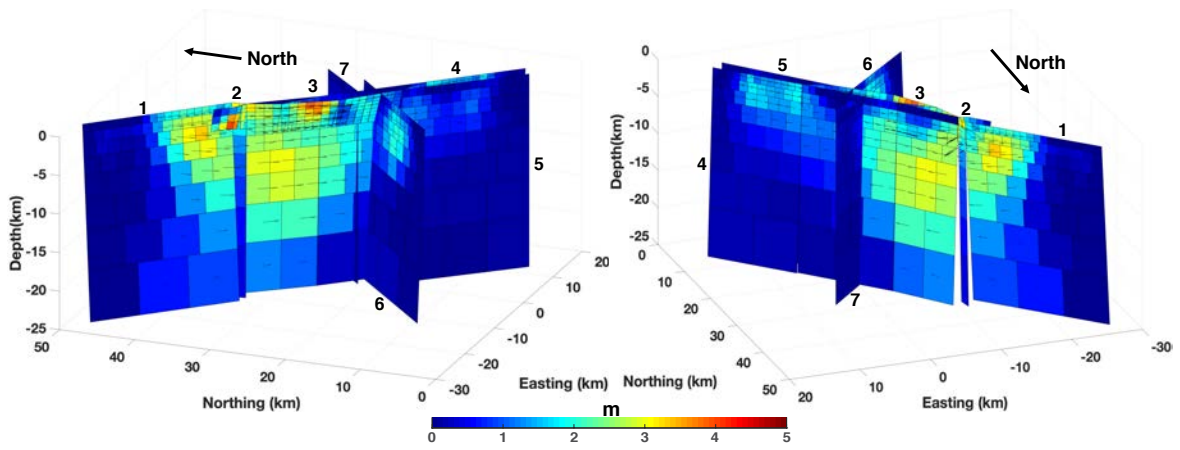
Figure 10: Slip distribution from the joint inversion of space geodetic data using a layered elastic half-space model. Notation is the same as in same as Figure 9. The calculated geodetic moment magnitude for the mainshock is M7.10.
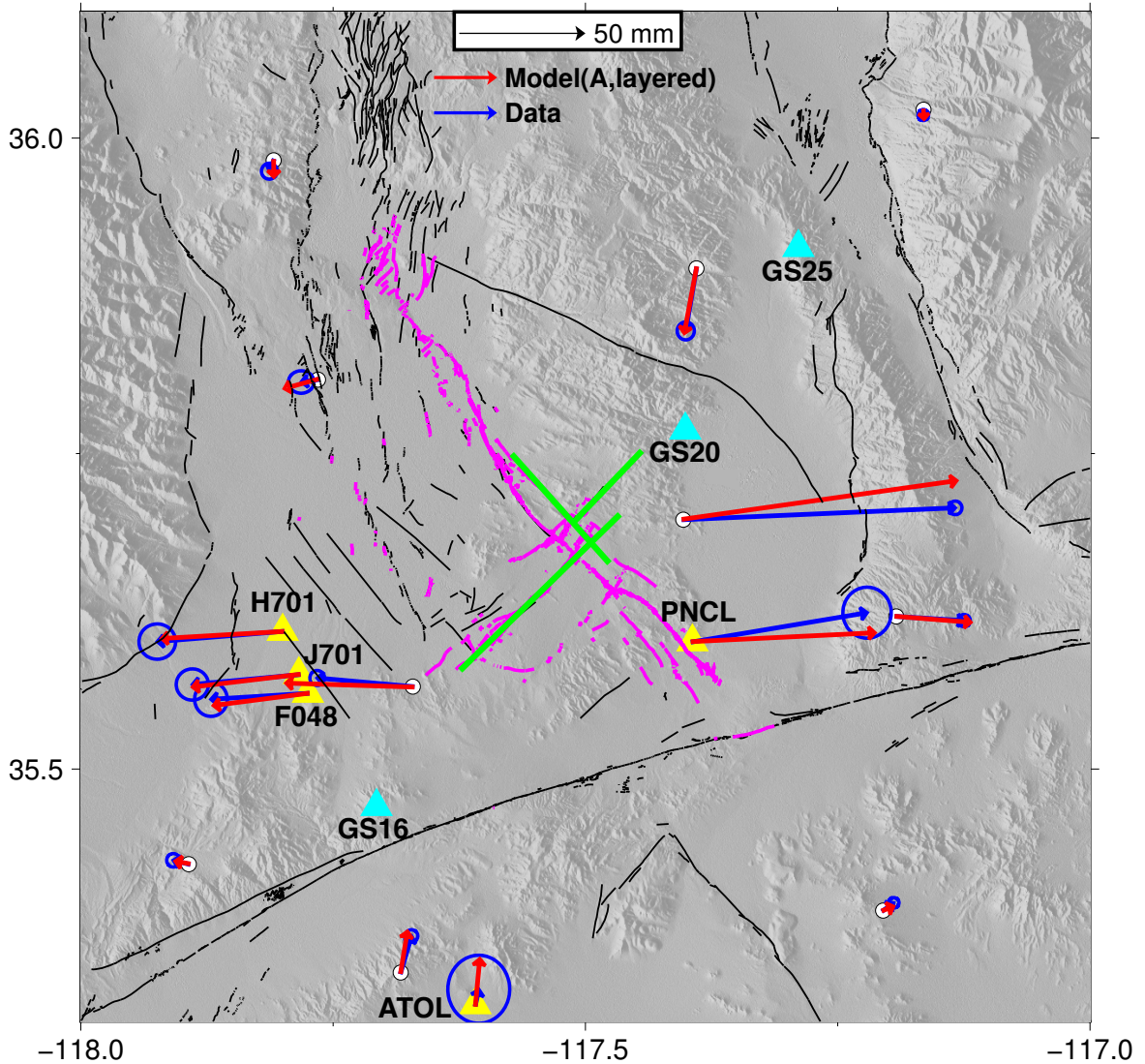
Figure 11: Observed (blue arrows) and modeled (red arrows) horizontal coseismic displacements due to the M6.4 foreshock. White circles denote the continuous and yellow triangles denote the campaign GNSS sites. Data are from Floyd et al. (2020). The ellipses show the 2-sigma errors. Green lines denote the modeled faults, including the left-lateral SW-trending fault segments 6, 7, and the right-lateral NW-trending fault segment 4 (see Figure 4a). Magenta lines represent surface traces of the 2019 earthquakes (Ponti et al., 2020), and black lines represent Quaternary faults (Jennings and Bryant, 2010).
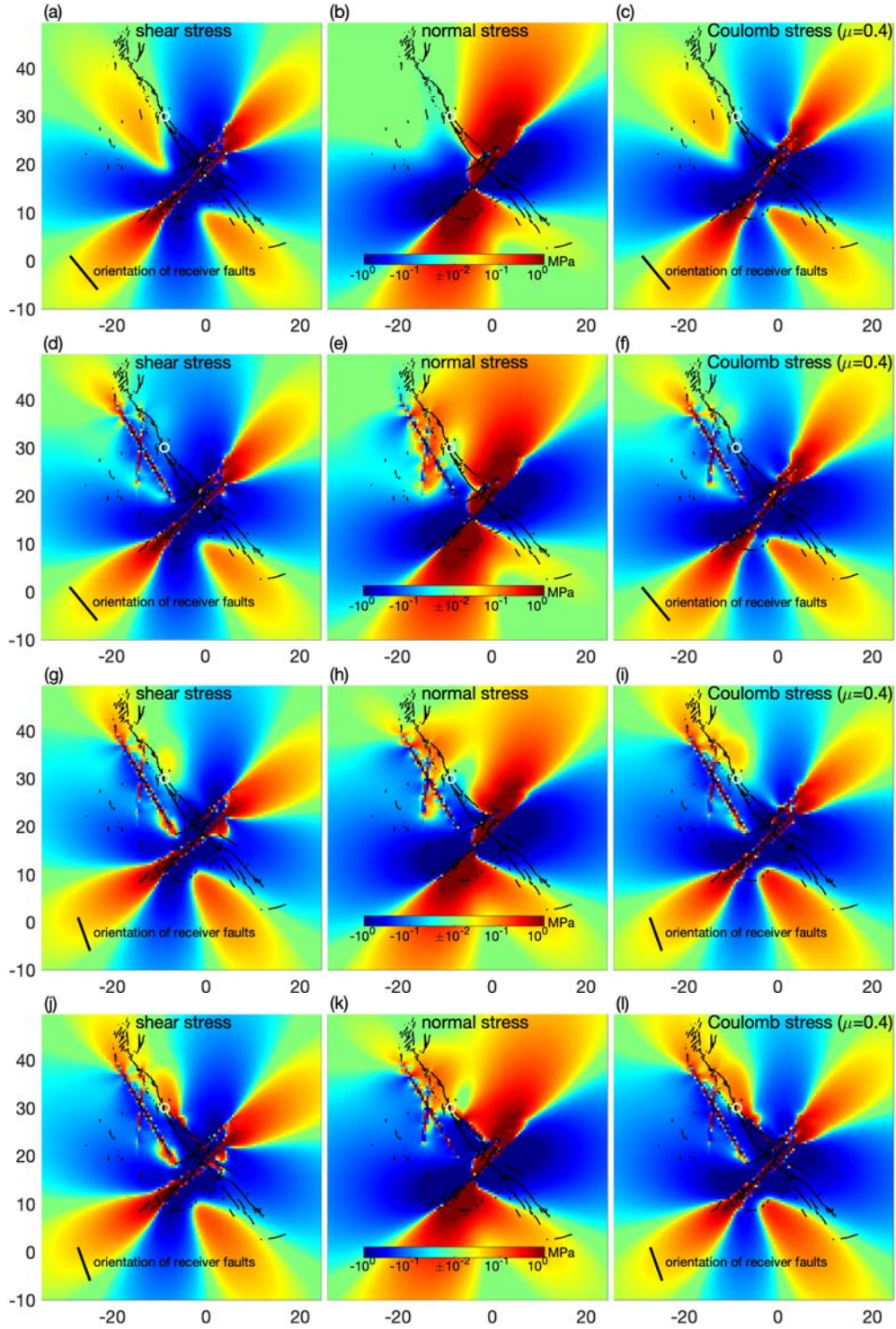
Figure 12: Static stress changes due to the pre-mainshock seismicity. Stress changes are computed at depth of 7 km. Top row (a-c): receiver faults striking 320° (average strike of the M7.1 mainshock). Second row(d-f): same as top row, plus stress changes from a pair of 1995 M5+ events. Third row(h-i): same as second row, for receiver faults striking 340° (consistent with the focal mechanism based on the first motion data). Bottom row(j-l): same as third row, but including the NW-striking segment (see Figure 11). The Coulomb stress change was calculated assuming the coefficient of friction of 0.4. White circle denotes the epicenter of the M7.1 mainshock. Orientation of receiver faults is shown by a black solid line. Black wavy line denotes the rupture trace.

34
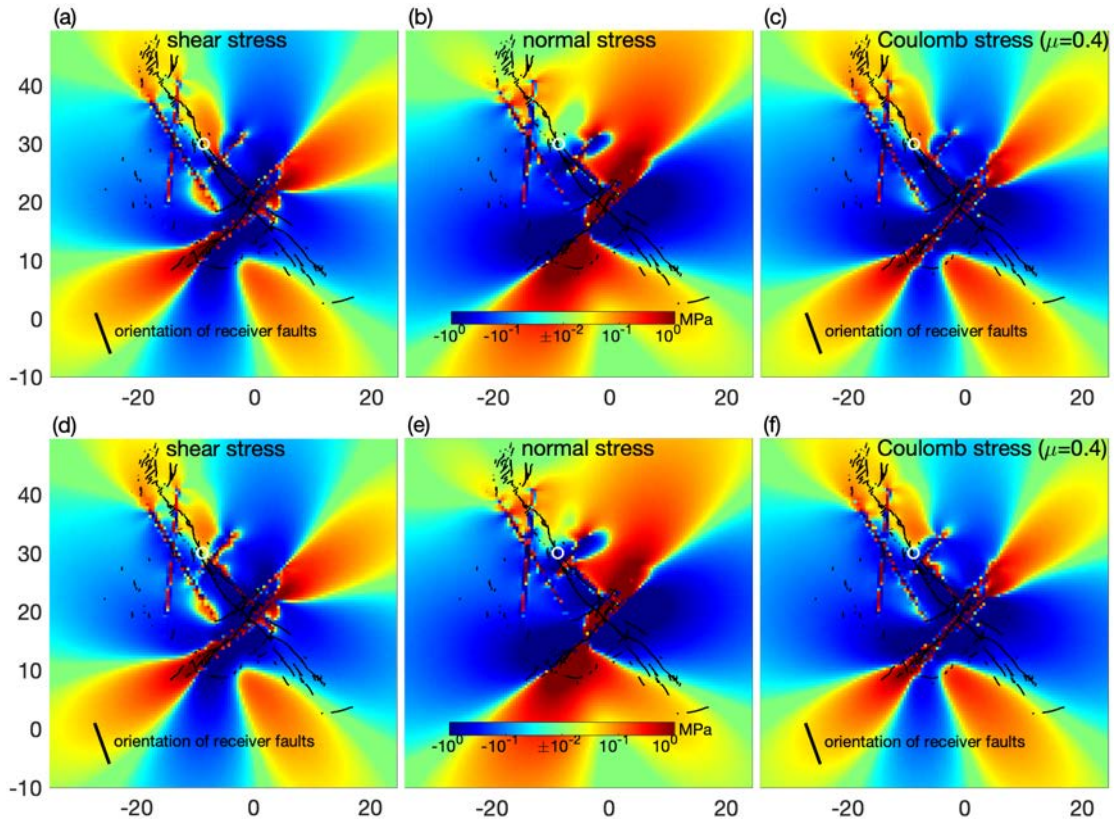
Figure 13: Same as in Figure 12, but including the 2019 M5.4 foreshock. The receiver fault strike is 340 degrees. Top row (a-c): The M5.4 event translated 2 km in SE direction with respect to the estimated moment centroid. Bottom row (d-f): The M5.4 event translated 2 km in NW direction with respect to the estimated moment centroid.
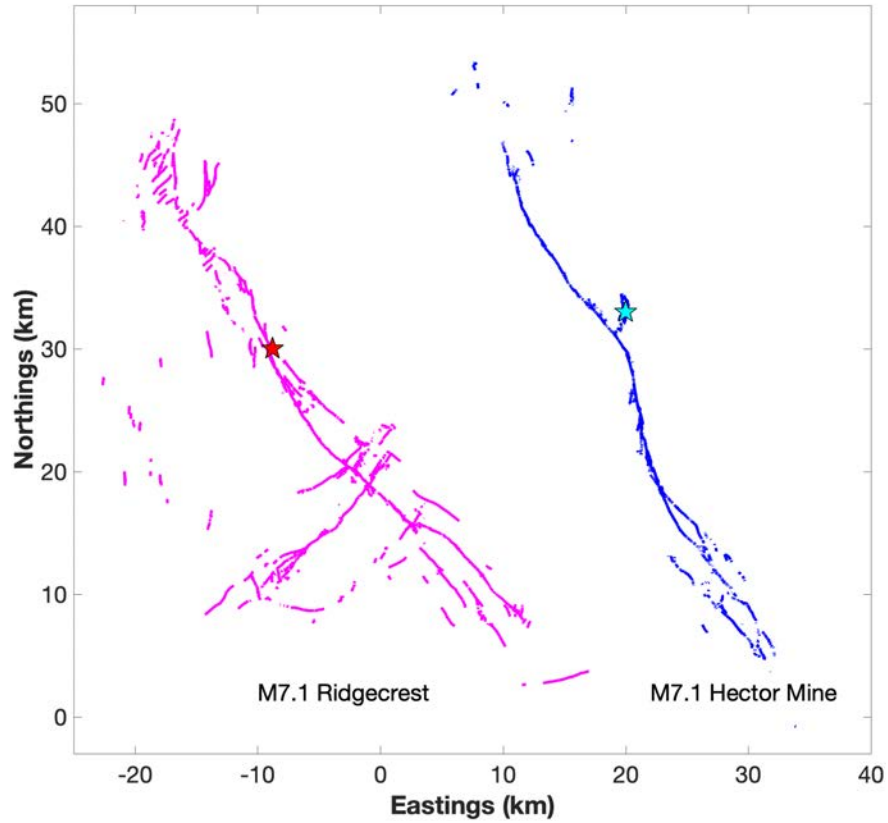
Figure 14: A comparison of the 2019 Ridgecrest and the 1999 Hector Mine rupture traces.
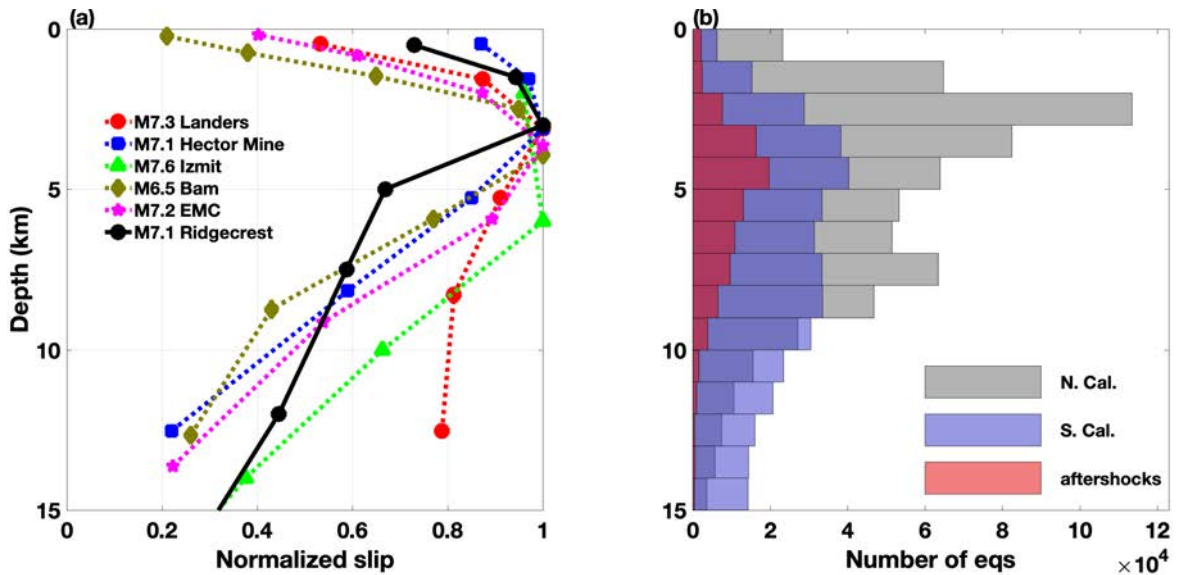
Figure 15: (a) Along-strike averaged coseismic slip as a function of depth for the July 5 M7.1 Ridgecrest earthquake (black solid line), as well as for several other M~ 7 strike-slip earthquakes (color dashed lines, data from Fialko et al. (2005b); Kaneko and Fialko (2011)). (b) Depth distribution of seismicity in California (see Data and Resources Section), and aftershocks of the 2019 Ridgecrest sequence (Ross et al., 2019). The magnitude completeness of the respective earthquake catalogs is 1-1.5.

Supplemental Material for

Finite slip models of the 2019 Ridgecrest earthquake sequence constrained by space geodetic data and aftershock locations

Zeyu Jin and Yuri Fialko
Institute of Geophysical and Planetary Physics, Scripps Institution of Oceanography, UC San Diego, La Jolla, CA, USA

Stress changes due to the 1995 M5+ earthquakes

In 1995 a sequence of earthquakes occurred in close proximity to the hypocenter of the 2019 M7.1 earthquake, with two events having magnitude greater than 5, and eight events with magnitude greater than 4 (e.g., Hauksson et al., 1995). To estimate stress changes caused by the largest events of the 1995 sequence, we generated slip models for the two M5+ earthquakes of the 1995 cluster. The rupture geometries were constrained using precisely relocated aftershocks of each of the M5+ events (Zhang and Lin, 2014). To obtain the coseismic displacement data, we generated interferograms using the ERS-1/2 SAR data from the descending tracks 170 and 442, and the ascending track 120 that span the epicentral area. We generated all possible interferometric pairs that have a perpendicular baseline less than 200 m, and acquisitions made within 2 years of the earthquake dates. We visually inspected all interferograms for the data quality and the signal to noise ratio. We selected independent interferograms that appear to be the least affected by noise, and averaged them to increase the signal to noise ratio. The averaged coseismic interferograms from each track were de-trended and sub-sampled using the same procedure as described in Section 3 in the main text. We jointly inverted the average LOS displacements for the slip distribution using the fault geometries derived from the aftershock data. The focal mechanisms and the geodetic moments corresponding to the best-fitting slip model were constrained to agree with seismic data. The data, best-fit models, and the residuals are shown in Figures S13 and S14. We then used the slip model for the M5+ 1995 earthquakes (Figure S14) to compute stress changes on vertical strike-slip faults of a given orientation. The results are shown in Figures S15 and S16 for particular fault strikes of 320 and 340 degrees, and in the on-line animations for the entire range of possible fault strikes, https://igppweb.ucsd.edu/~fialko/ridgecrest.html.
A combined effect of static stress changes due to the 1995 events and 2019 events can be easily computed using superposition.

We also estimated dynamic stress changes due to the 2019 July 5 M5.4 left-lateral strike-slip event using an analytic solution for a point source in a whole elastic space (Aki and Richards, 1992, chapter 4.3). First, we calculated synthetic seismograms using the following input parameters: rupture strike of 39 degrees, rupture duration of 1s, shear modulus of 33 GPa, Poisson's ratio of 0.25, and density of 3×10^3 kg/m^3. We numerically differentiated the displacement time series to calculate components of the strain tensor, and used Hooke's law to

compute components of the stress tensor. The latter were resolved on a vertical plane representing a target fault to obtain time series of the normal and shear stress. The dynamic Coulomb stress change was then computed assuming the coefficient of friction of 0.4. At each point, we kept track of the maximum dynamic Coulomb stress change for right-lateral slip on a NW-striking target fault. Figure S17 shows the computed maximum dynamic Coulomb stress change around the hypocenter of the 2019 M7.1 earthquake, assuming the target fault strike of 340 degrees.

List of Figure Captions

Figure S1 illustrates the selection of relative weighting between each dataset and model smoothness used in the inversions.

Figure S2 shows how the misfit varies as a function of the assumed dip angle for each major fault.

Figure S3 shows the individual segments approximating the shallow splay faults.

Figure S4 shows a comparison of seismicity distributions from Ross et al. (2019) and Shelly (2019) relocated catalogs, and locations of the modeled fault segments with respect to the detected aftershocks.

Figure S5 shows how the misfit varies as a function of the assumed dip angle for each splay fault.

Figure S6 shows the sub-sampled data, best-fitting models and residuals for the ALOS-2 Line of Sight (LOS) displacements.

Figure S7 shows the sub-sampled data, best-fitting models and residuals for the Cosmo-Skymed azimuth offsets.

Figure S8 shows the difference between homogeneous and layered half-space models and the comparison of surface displacements between the cGNSS data and each model prediction.

Figure S9 presents results of the model resolution tests.

Figures S10 & S11 show the slip distribution from the joint inversion of space geodetic data for Model B (assuming a homogeneous and layered elastic half-space models respectively).

Figure S12 shows the observed and predicted horizontal displacements due to the M6.4 foreshock assuming slip on the left-lateral fault segments only.

Figure S13 shows the sub-sampled data, best-fitting models and residuals for the 1995 M5+ earthquakes.

Figure S14 shows the inferred slip distribution for a pair of the 1995 M5+ earthquakes, assuming a layered elastic half-space model.

Figure S15 shows the stress changes due to the 1995 M5 Ridgecrest sequence, for receiver faults striking at 320 degrees.

Figure S16 shows the static stress changes due to the 1995 M5 Ridgecrest sequence, for receiver faults striking at 340 degrees.

Figure S17 shows the maximum dynamic Coulomb stress changes due to the 2019 July 5 M5.4 earthquake, for receiver faults striking at 340 degrees.

Data and Resources

First motion focal mechanism of the 2019 M7.1 mainshock is available at https://earthquake.usgs.gov/earthquakes/eventpage/ci38457511/focal-mechanism, last accessed Nov 2019.

Seismic moment of the 2019 M7.1 mainshock is available at https://earthquake.usgs.gov/earthquakes/eventpage/ci38457511/moment-tensor, last accessed Nov 2019.

Seismic moment of the 2019 M6.4 foreshock is available at https://earthquake.usgs.gov/earthquakes/eventpage/ci38443183/moment-tensor, last accessed Nov 2019.

Seismic moment of the 2019 M5.4 foreshock is available at https://earthquake.usgs.gov/earthquakes/eventpage/ci38450263/moment-tensor, last accessed Nov 2019.

We have used parametric data and focal mechanisms from the Caltech/USGS Southern California Seismic Network (SCSN), doi:10.7914/SN/CI; stored at the Southern California Earthquake Data Center (SCEDC), doi:10.7909/C3WD3xH1. Waveform relocated earthquake catalog for southern California is available at https://scedc.caltech.edu/research-tools/alt-2011-yang-hauksson-shearer.html, last accessed Nov 2019. Double-difference relocated earthquake catalog for northern California is provided by the Northern California Earthquake Data Center (NCEDC), doi:10.7932/NCEDC, available on-line at https://www.ncedc.org/ncedc/catalog-search.html, last accessed Nov 2019.

Movies of stress changes due to the largest foreshocks of the 2019 sequence, and the 1995 earthquakes, spanning all possible fault strikes, are available at the following URL: https://igppweb.ucsd.edu/~fialko/ridgecrest.html

References

Aki, K. and Richards, P.G. (2002). Quantitative Seismology, 700 pp. *Univ. Sci. Books, Sausalito, Calif*.

Hauksson, E., Hutton, K., Kanamori, H., Jones, L., Mori, J., Hough, S., & Roquemore, G. (1995). Preliminary report on the 1995 Ridgecrest earthquake sequence in eastern California. *Seismological Research Letters*, *66*(6), 54-60.

Zhang, Q., & Lin, G. (2014). Three-dimensional Vp and Vp/Vs models in the Coso geothermal area, California: Seismic characterization of the magmatic system. *Journal of Geophysical Research: Solid Earth*, *119*(6), 4907-4922.
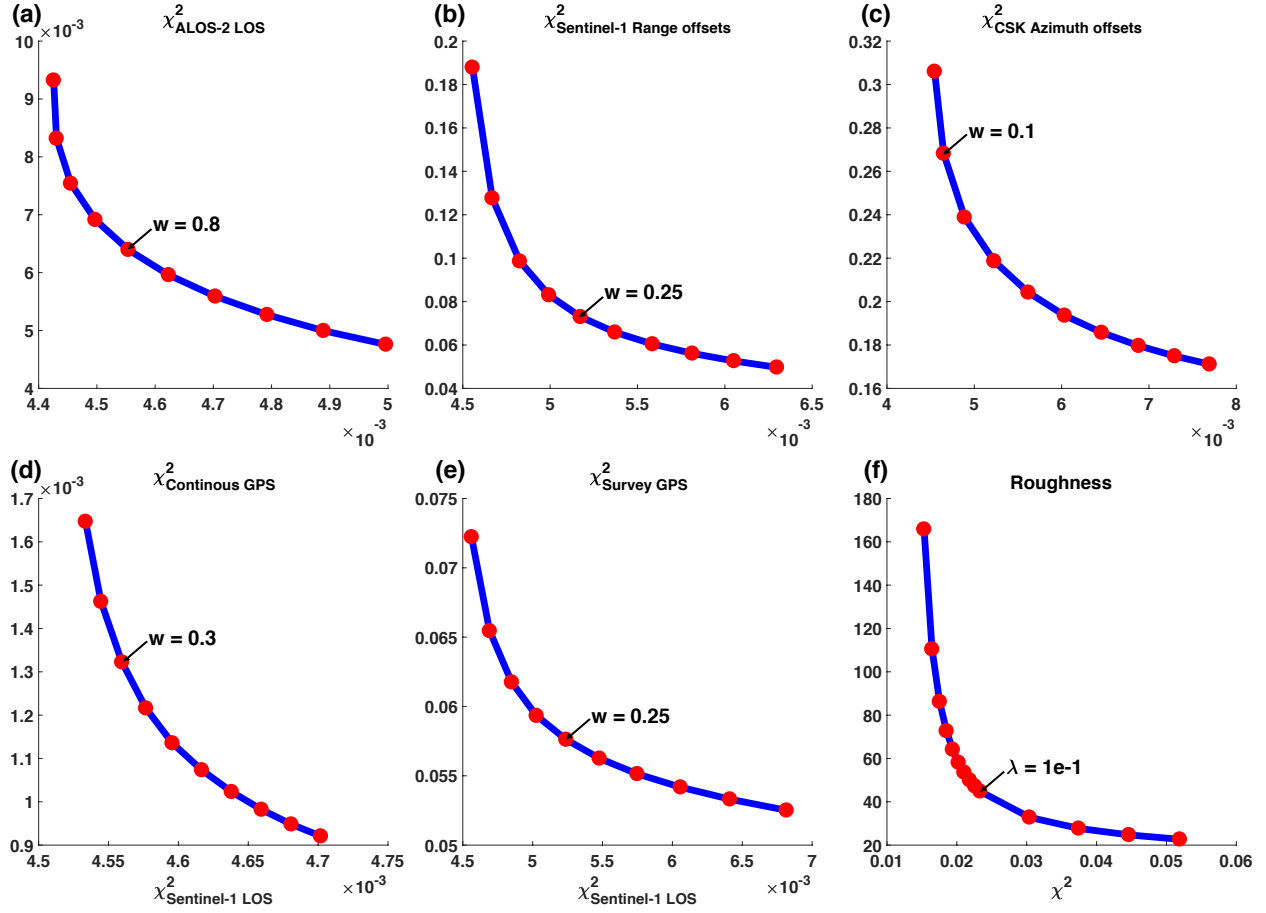
Figure S1: Chi-squared misfits for different data sets used in the joint inversion, plotted against the chi-squared misfit for Sentinel-1 LOS displacement data. The latter are assigned a relative weight of 1. The preferred relative weight (w) for other data sets is denoted by an arrow, with a numerical value provided. (a) ALOS-2 LOS displacements, (b) Sentinel-1 range offsets, (c) Cosmo-Skymed azimuth offsets, (d) continuous GNSS/GPS, (e) campaign GNSS/GPS. Because the Cosmo-Skymed azimuth offsets are noisy compared to other datasets (see Figure 2 in the main text), they are relatively down-weighted to preclude misfits to other data sets. (f) A trade-off curve of the model misfit versus the model roughness $1/\lambda$. The inversion was minimized using an objective function $F(m, \lambda) = ||Gm - d|| + \lambda||Lm||$, where G is the matrix of the Green's functions, m is the vector of unknown (strike-s & dip-) slip components, d is the data vector, L is the first-order Tikhonov's regularization matrix, λ is the smoothness factor.
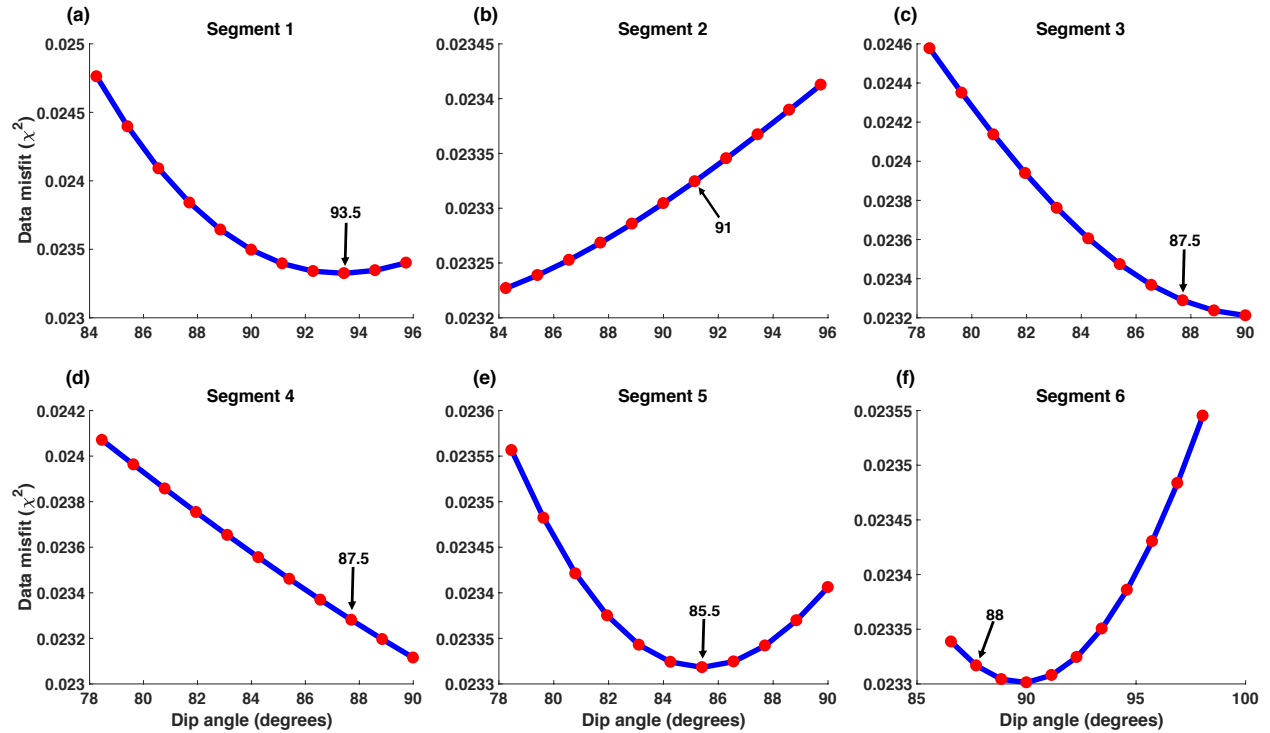
Figure S2: Sensitivity of the data misfit to the assumed values of dip angles for each major fault segment (see solid black lines and segment numbers in Figure 3 in the main text). The dip angles corresponding to the preferred model (Model A) are denoted by an arrow, with a numerical value provided. At each step we recalculated the appropriate Green's functions, and evaluated the weighted least square residual between the model and the data. The misfit for all 6 segments is not sensitive to small changes in the dip angle, with the largest difference between misfits of less than 1.5%. For fault segments 1, 5, 6, the dip angle corresponding to a minimum in the misfit curves coincides with the dip angle estimated using the aftershock data. For fault segments 2, 3, 4, there is no well-defined minimum, and we use dip angles estimated from the aftershock data.

6
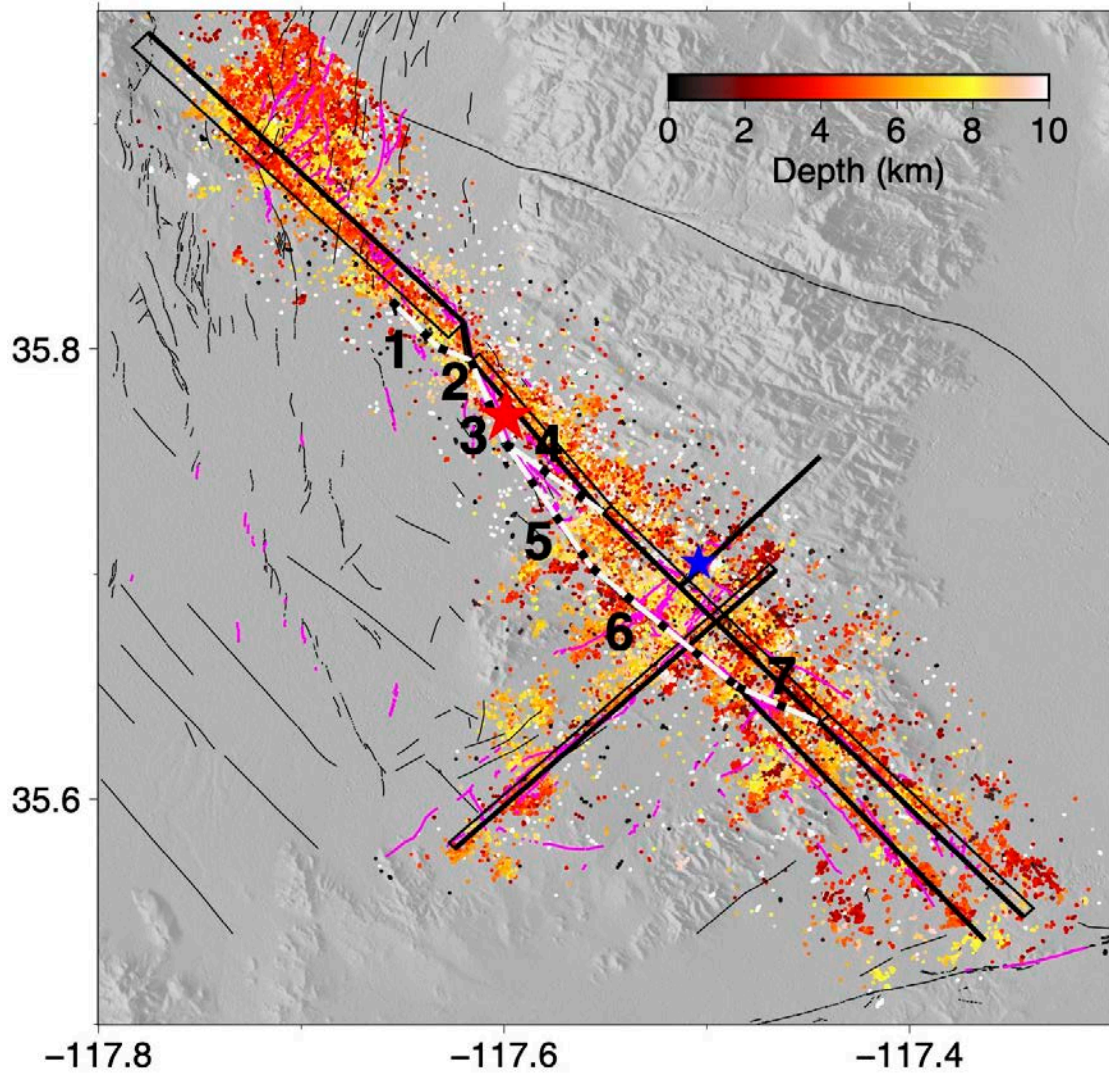
Figure S3: Numbers denote individual rectangular segments used to approximate shallow splay faults. Other notation is the same as in Figure 3a in the main text.
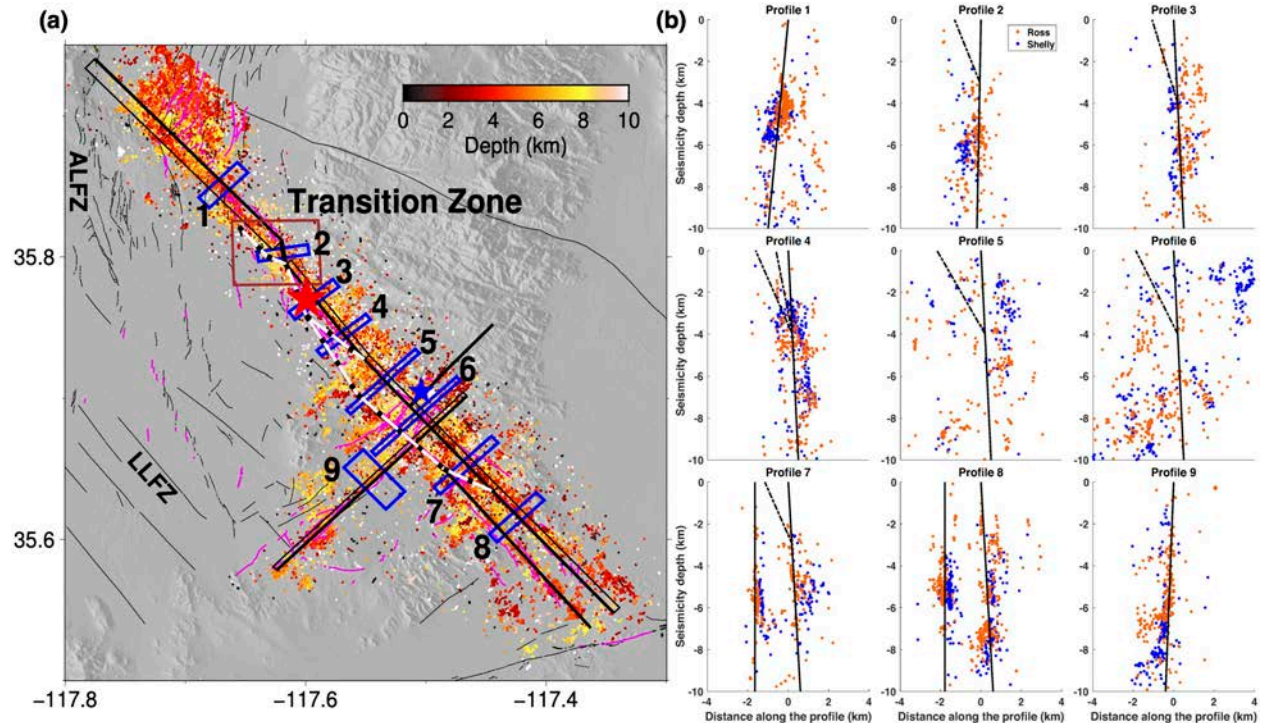
Figure S4: (a) Map view of aftershocks produced by the Ridgecrest events. The notation is the same as in Figure 4 in the main text. Here we include a few additional cross-sections. (b) Cross-section profiles showing seismicity distributions from Ross et al. (2019) and Shelly (2019), and locations of the modeled fault segments from our preferred fault model (Model A). LLFZ = Little Lake Fault Zone; ALFZ = Airport Lake Fault Zone.
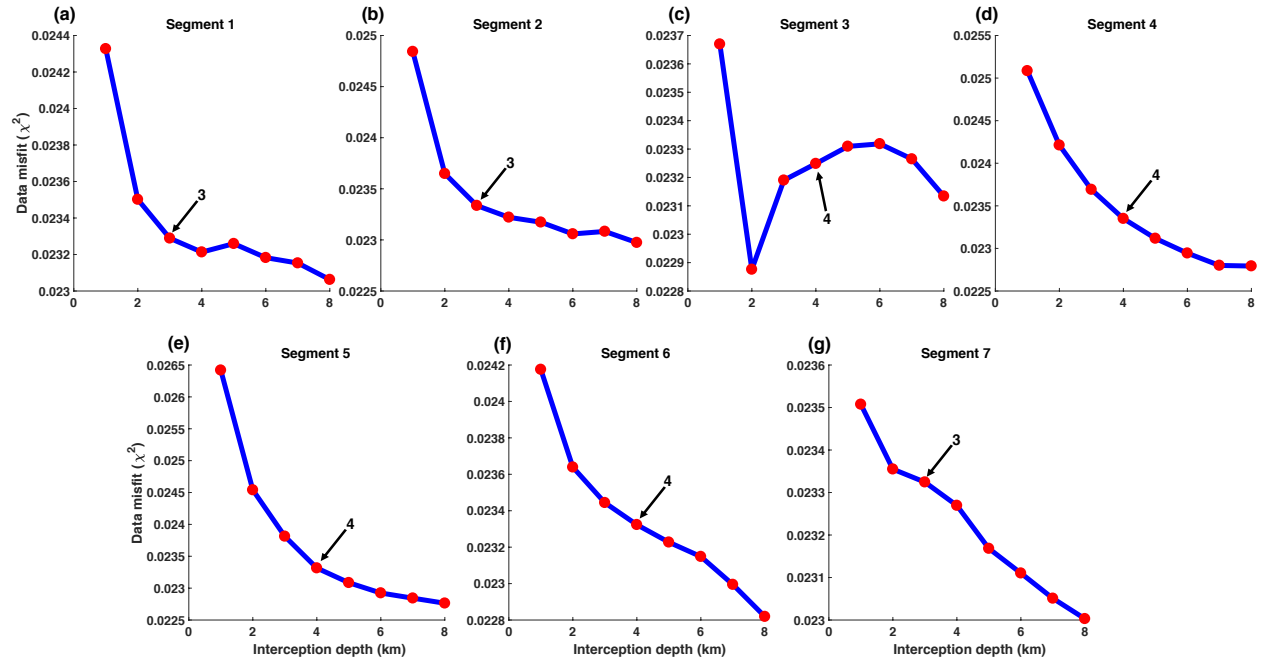
Figure S5: Results of a grid search for the best-fit dip angles of shallow splay faults. Segment numbers are indicated in Figure S3. The fault dip is parameterized by the depth of intersection between the splay fault and the main fault (defined by a linear fit to the aftershock cloud). The preferred interception depth of each segment is denoted by an arrow, with a numerical value provided. The misfit is not sensitive to small variations in the dip angles of the shallow splay faults (the largest difference in misfits is less than 3%). Given no strong constraints from the geodetic data, we assumed that splay faults connect to the top of the aftershock cloud at depth of ~3-4 km (Figure 3b in the main text).
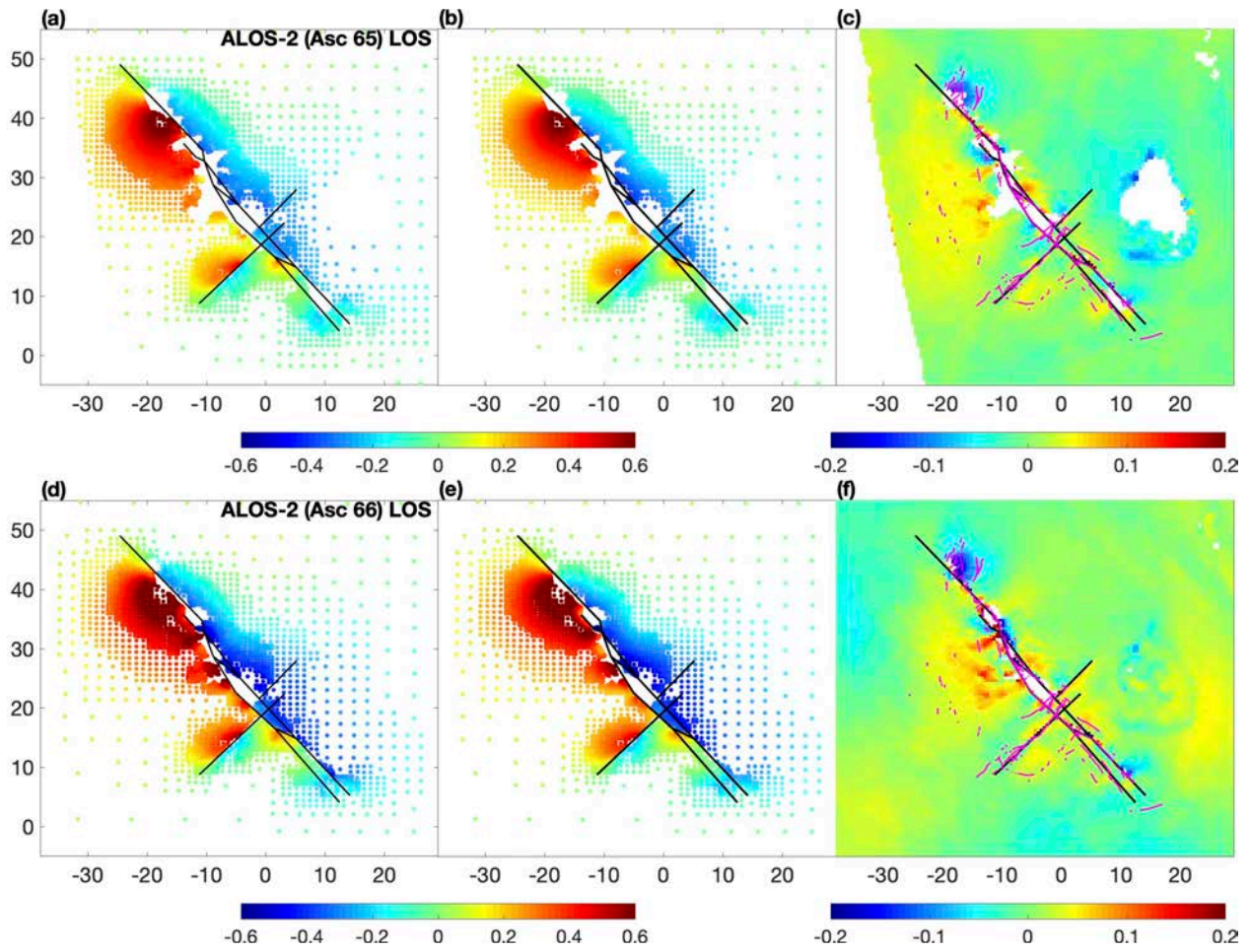
Figure S6: (a,d) Sub-sampled data, (b,e) best-fitting models, and (c,f) residuals for the ALOS-2 LOS displacements from the ascending tracks 65 (a-c), and 66 (d-f). Colors denote the amplitude of LOS displacements, in m. Other notation is the same as in Figure 6 in the main text.
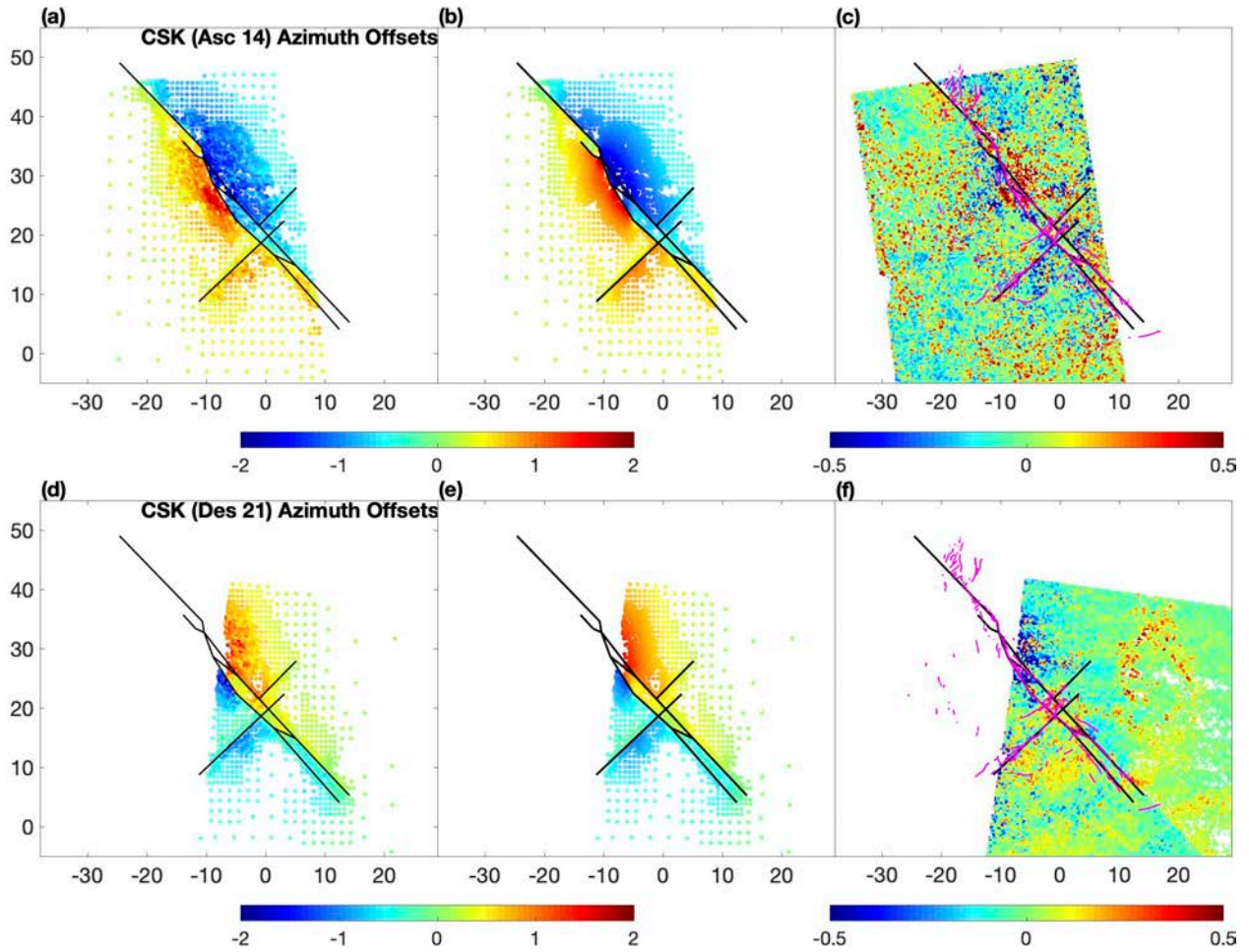
Figure S7: (a,d) Sub-sampled data, (b,e) best-fitting models, and (c,f) residuals for the Cosmo-Skymed azimuth offsets from the ascending track 14 (a-c), and descending track 21 (d-f). Colors denote the amplitude of azimuth offsets, in m. Other notation is the same as in Figure 6 in the main text.
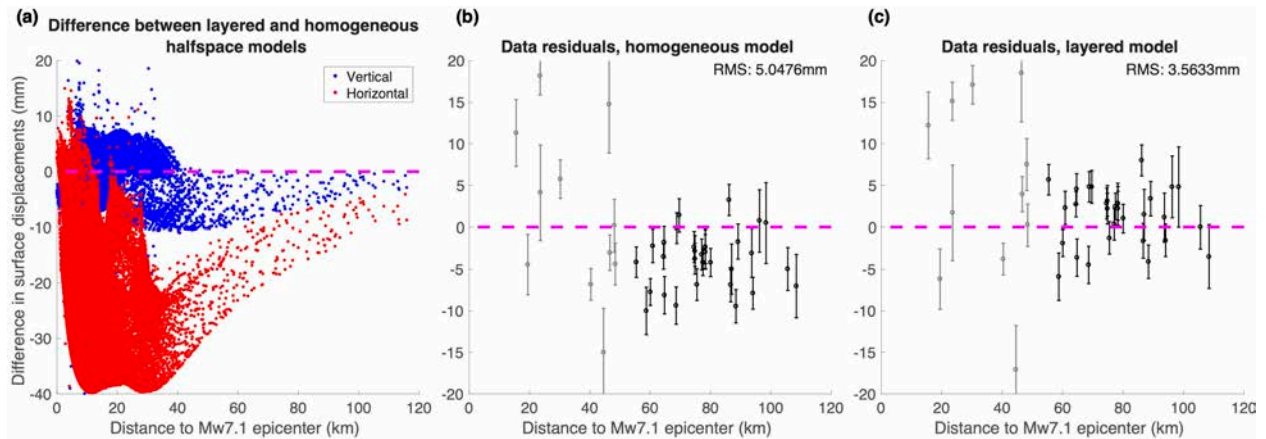
Figure S8: (a) The difference between surface displacement predicted by the layered and homogeneous half-space models. The difference is computed at the sub-sampled data points used in the inversion. (b,c) The difference between the observed (cGNSS) and modeled horizontal displacements for (b) homogeneous and (c) layered half-space models. The near-field data points (within 50km from the Mw7.1 epicenter) are plotted in gray, and the far-field data points are plotted in black. The RMS values of the residuals correspond to the far-field data. The residuals indicate that the homogeneous model has a small but systematic bias in the far field (over-predicting the data), while the layered model has a more realistic asymptotic behavior.
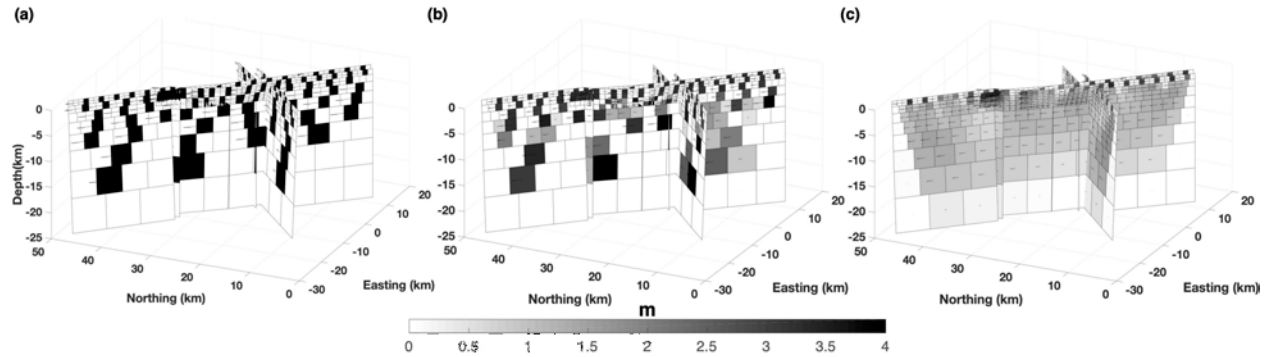
Figure S9: Model resolution tests. (a) Synthetic input slip model, (b) inverse model without imposed smoothing but with positivity constraints on both strike and dip slip components, (c) inverse model with smoothing (same parameters as used in deriving the best-fit model, see Figures 9 and 10). The input model assumes a pure left-lateral strike-slip of 4 meters at arbitrarily chosen slip patches. The synthetic data were calculated at the locations of data points in the resampled LOS and AZO maps from the ascending and descending orbits (see Figures 6 and 7), and at the GPS sites (see Figure 8). A simulated atmospheric noise was added to the synthetic data, where its amplitude was scaled such that the RMS (Root Mean Square) value was the same as the maximum RMS value of the residual (See Figure 6c,f) of the co-seismic interferograms in the far field.
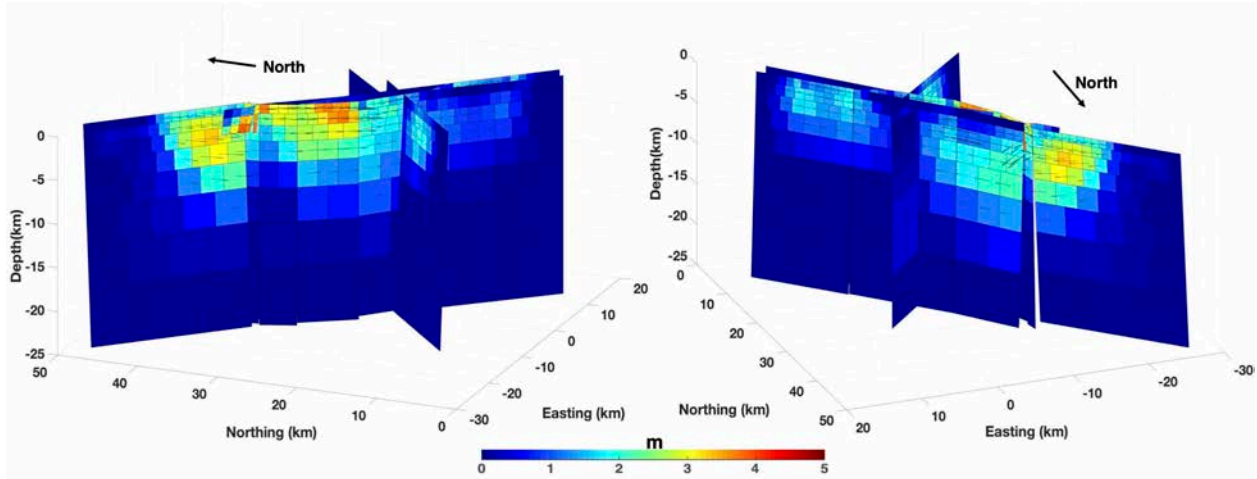
Figure S10: The slip distribution from the joint inversion of space geodetic data using a homogeneous elastic half-space, for an alternative fault geometry (Model B) assuming a sub-vertical fault instead of the shallow splay faults (see Figures 4 and S3). Notation is the same as in Figure 9.
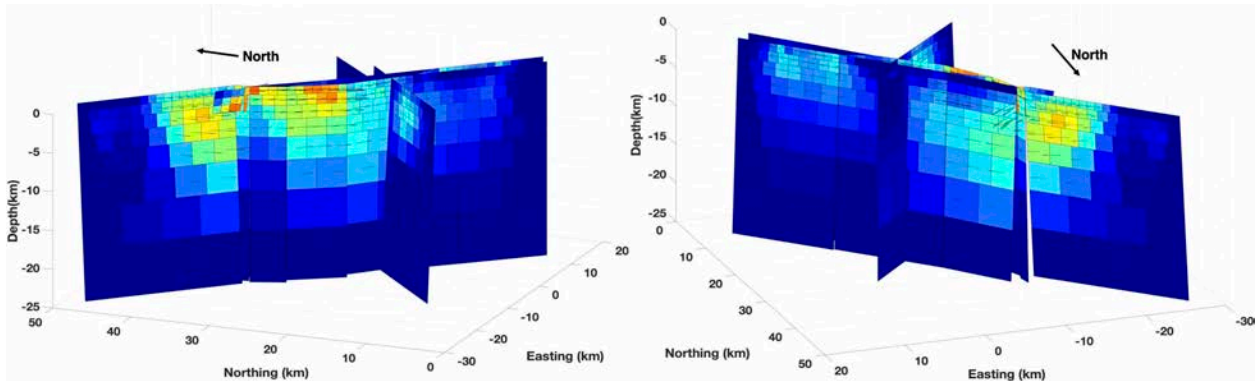

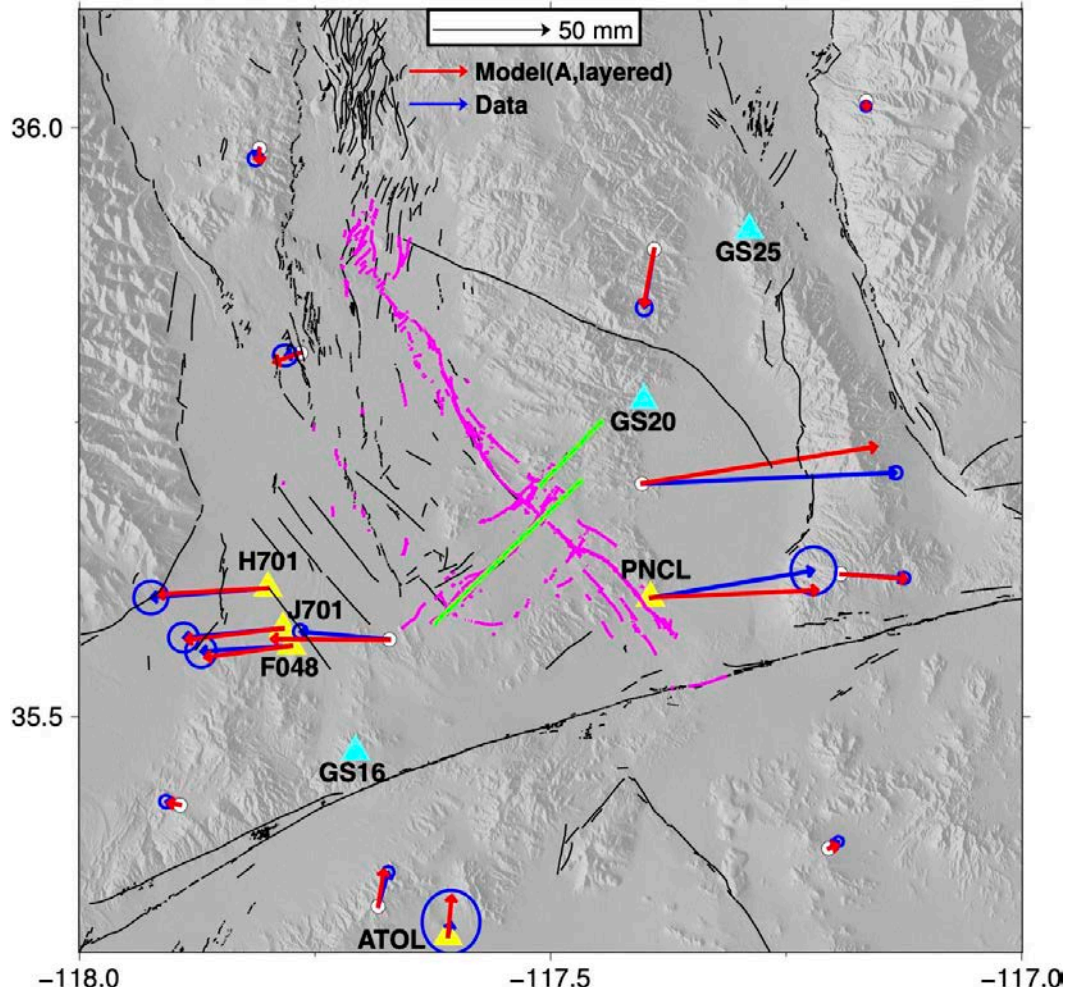Figure S11: Same as Figure S11, assuming a layered elastic half-space model.

14

Figure S12: Coseismic displacements due to the M6.4 foreshock observed by the continuous (white dots) and campaign (yellow triangles) GNSS sites and predictions of the best-fit layered model assuming slip on the left-lateral NE-trending fault segments 6 and 7 (green lines, also see Figure 4). The ellipses show the 2-sigma errors. Other notation is the same as in Figures 8 and 11.
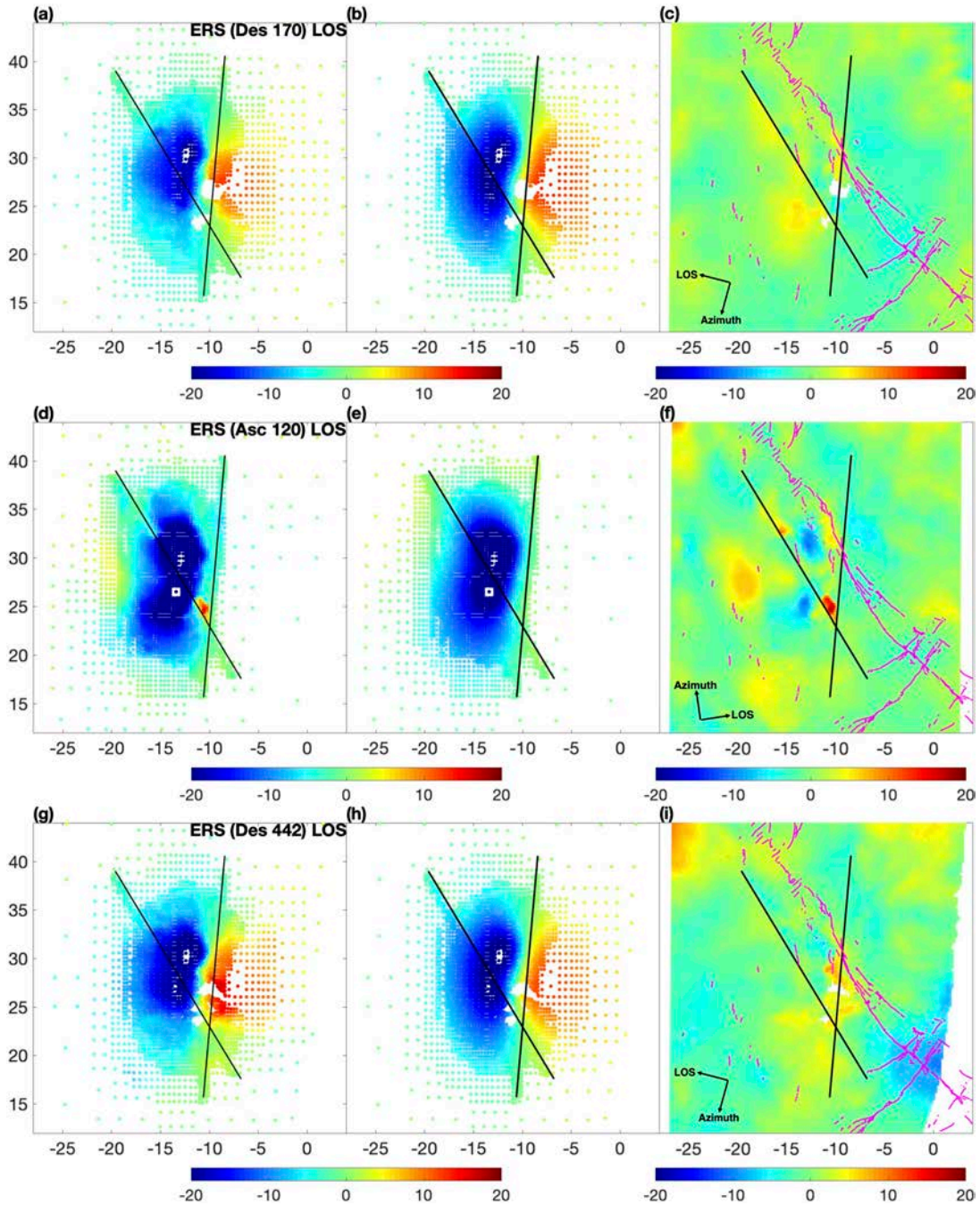
Figure S13: (a,d,g) Sub-sampled data, (b,e,h) best-fitting models, and (c,f,i) residuals for the ERS radar interferograms from the descending track 170 (a-c), ascending track 120 (d-f) and descending track 442 (g-i). Colors denote the amplitude of LOS displacements in mm. Motion toward the satellite is deemed positive. Black lines denote the projected surface traces of the two M5+ earthquakes that occurred in 1995. Magenta lines represent surface rupture traces of the 2019 earthquakes.
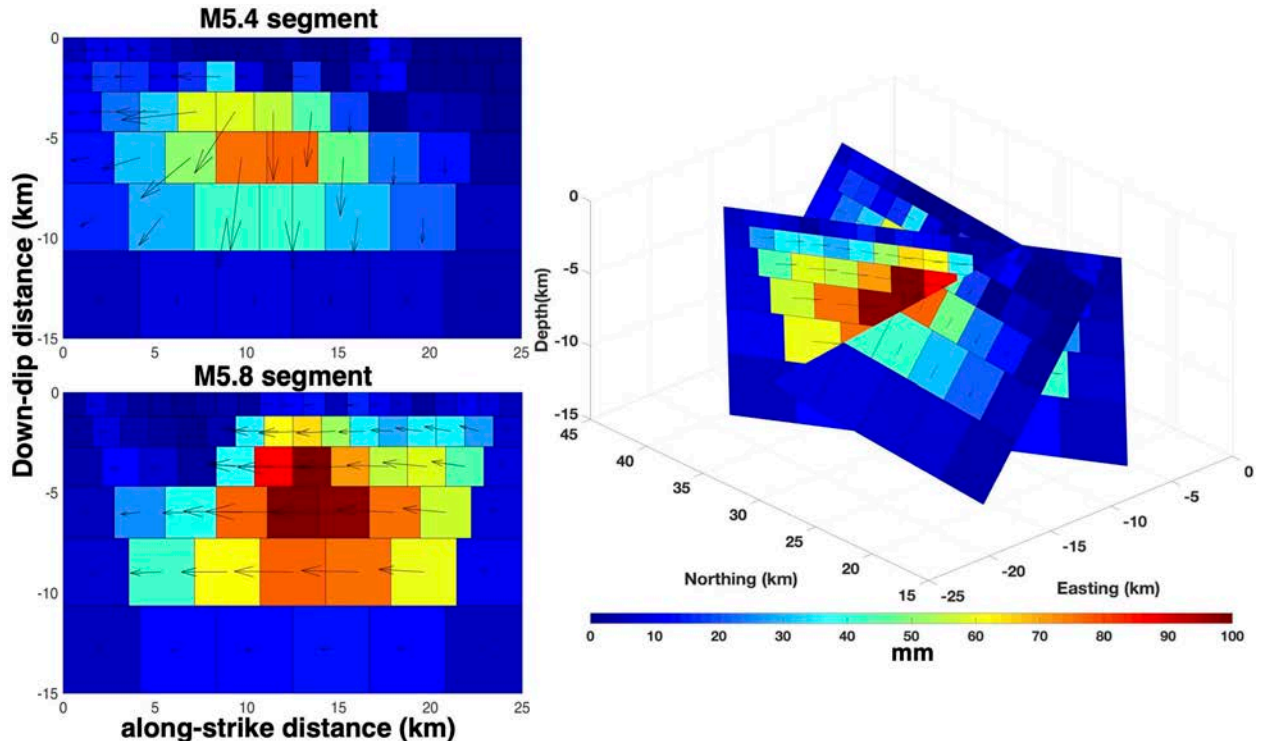
Figure S14: The best-fit slip distributions for the two 1995 M5+ earthquakes derived from the joint inversions of the ERS data (see Figure S13) using a layered elastic half-space model. Notation is the same as in Figure 9. The M5.4 earthquake involved normal faulting and some right-lateral slip. The M5.8 earthquake had a predominantly right-lateral strike-slip focal mechanism.
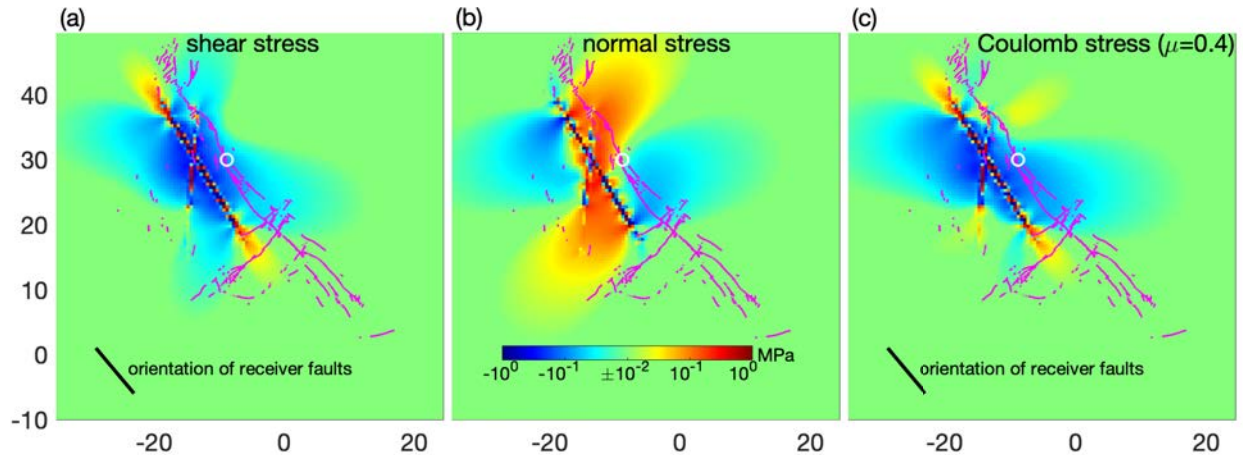
Figure S15: Coseismic stress changes due to a pair of M5+ Ridgecrest earthquakes that occurred in 1995. The Coulomb stress change was calculated assuming a coefficient of friction of 0.4, at a depth of 7km. White circle denotes the epicenter of the M7.1 2019 mainshock. Orientation of receiver faults (strike of 320 degrees) is shown by a black solid line. Magenta wavy line denotes the rupture traces of the 2019 earthquakes.
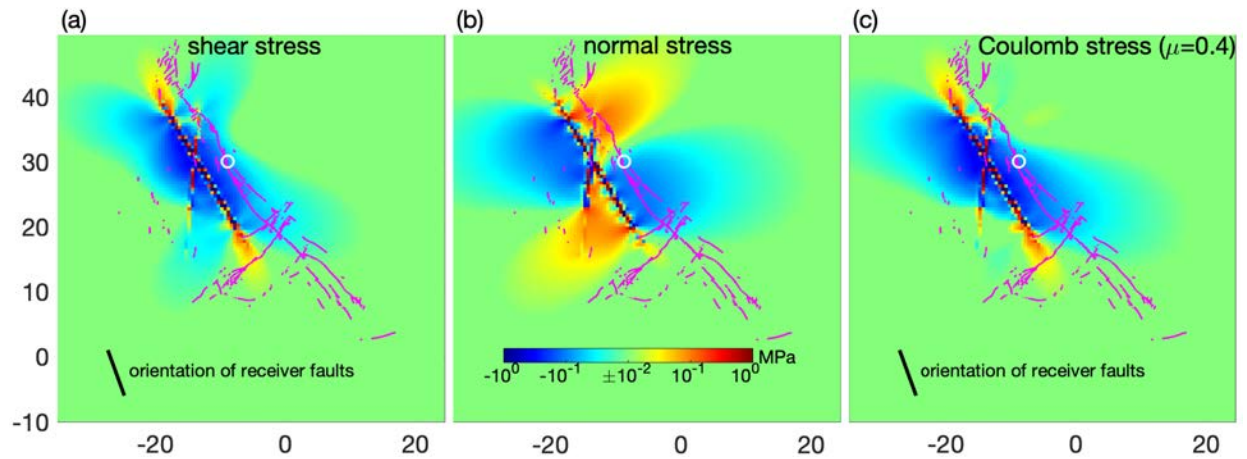

Figure S16: Same as Figure S15, for receiver faults striking at 340 degrees.
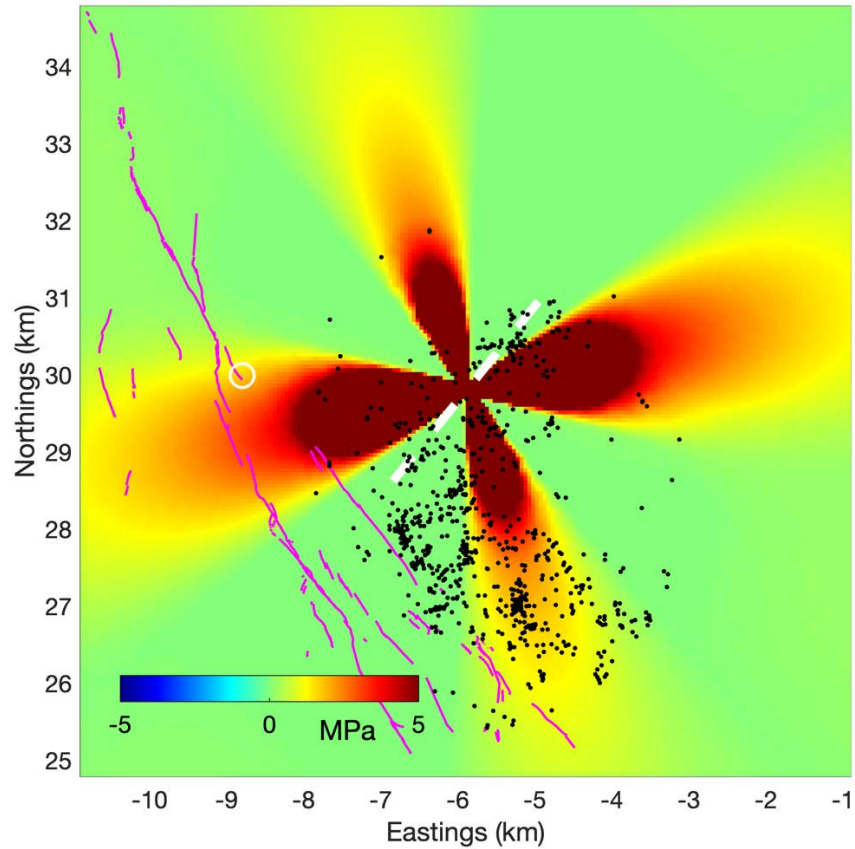
Figure S17: Maximum dynamic Coulomb stress changes for right-lateral slip on vertical receiver faults striking 340 degrees due to a point source representing the 2019 July 5 M5.4 foreshock. The orientation of the rupture plane of the foreshock is shown by a white dashed line, and the M7.1 hypocenter is shown by a white circle. Black dots denote seismicity that occurred between the M5.4 foreshock and the M7.1 mainshock. Magenta lines denote the surface rupture of the 2019 earthquakes. Dynamic stresses of a comparable magnitude were also produced by the July 4 M6.4 foreshock.